J. Fluid Mech. (2006), *vol.* 550, *pp.* 251–288.
doi:10.1017/S0022112005008207 Printed in the United Kingdom

Transient growth of perturbations in a vortex column

By D. S. PRADEEP AND F. HUSSAIN

Department of Mechanical Engineering, University of Houston, Houston, TX 77204-4006, USA

(Received 9 April 2005 and in revised form 24 August 2005)

Linear transient growth in a normal-mode-stable vortex column is studied by extracting 'optimal modes' of perturbations. Amplifications occur over a wide range of azimuthal wavenumbers m and axial wavenumbers k, and can be more than three orders of magnitude even at moderate vortex Reynolds numbers Re (checked up to 10^4). Transient growth is unbounded in the inviscid limit. For given Re and k, axisymmetric ($m=0$) modes undergo the largest volume-integrated energy growth, whereas maximum core energy growth occurs for bending waves ($|m|=1$). At fixed m and Re, growth decreases with increasing k, due to the damping effect of viscosity. At fixed m and k, growth increases rapidly with Re – pointing to the significance of transient growth in high-Re practical flows, such as the trailing vortex. Inviscid effects not only cause transient growth, but also its subsequent arrest. There are two distinct mechanisms for growth. First, two-dimensional perturbations amplify because the streamlines have 'positive tilt', contributing $uv>0$ stress necessary for growth; here u and v are the radial and azimuthal velocity perturbations, respectively. Second, three-dimensional perturbations grow through azimuthal stretching of spiral vortex filaments containing radial vorticity. Decay in both cases is due to the differential advection – of axial vorticity by the mean swirl – transforming the perturbation streamlines to predominantly 'negative tilt', producing $uv<0$ stress. The transient growth mechanism is explained in terms of the distinct effects of the strain and vorticity components of the mean flow, which play counteractive roles. While strain amplifies energy, vorticity limits transient growth by inducing wave motions, in which radial vorticity is depleted by vortex line coiling, i.e. by the tilting of radial vorticity into axial and azimuthal components. Since the strain-to-vorticity ratio varies with radius in the vortex, the competition between strain and vorticity selects a preferred radius of localization of an 'optimal perturbation'. With increasing growth, axisymmetric optimal modes are localized at progressively larger radii and their growth rates progressively diminished – both limiting the physical significance of such modes in high-Re practical flows. An optimal bending wave, on the other hand, is localized closer to the vortex column, where a vorticity perturbation external to the core can resonantly excite vortex core waves. This leads to substantial growth of core fluctuation energy and, probably, to core transition to turbulence. Such resonant growth may be the mechanism for the appearance of bending waves in a vortex in a turbulent field.

1. Introduction

Well-organized, elongated vortices (coherent structures, CS) commonly occur in turbulent flows and dominate phenomena of technological interest, such as entrainment, mixing, drag, and aerodynamic sound. In the case of the aircraft wake, intense trailing vortices pose a hazard to trailing aircraft. The importance of predicting CS evolution has motivated numerous studies of fundamental vortex dynamics, including pairing, reconnection, breakdown, vortex–turbulence interaction, and instability. The bulk of the existing work on linear stability analysis of a vortex has focused on normal modes, i.e. perturbations that grow or decay exponentially in time. Many types of normal-mode instability mechanisms are now well-understood, e.g. the centrifugal instability (see Sreedhar & Ragab 1994), the elliptical instability (Kerswell 2002), and instability in the presence of strong axial flow (Mayer & Powell 1992).

The present work focuses on the growth of small-amplitude perturbations in an Oseen vortex, with velocity profile of the form

$$V = \left(1 - \mathrm{e}^{-r^2}\right)/r, \tag{1.1}$$

where V is the azimuthal velocity and r the radius. An isolated Oseen vortex – representative of an individual large-scale vortex in numerous flows of practical interest (such as mixing layers and plane wakes) – is centrifugally stable, has no axial flow, and is not subjected to any external strain; the aircraft trailing vortex is also essentially free from these effects. None of the instability mechanisms mentioned above are operative, and the vortex is normal-mode stable; see e.g. Lessen, Singh & Paillet (1974) and Michalke & Timme (1967). Lessen *et al.* consider the stability of the q-vortex and show that the vortex is stabilized when q (swirl-to-axial velocity ratio) exceeds ≈ 1.5. The Oseen vortex corresponds to the $q \to \infty$ limit and hence is stable. Michalke & Timme consider the inviscid stability of centrifugally stable, axisymmetric vortex profiles and show that normal-mode instability is possible only when the mean vorticity has an extremum at $r > 0$. Again, this shows the normal-mode stability of the Oseen vortex.

Normal-mode stability, however, does not imply that perturbations cannot grow, because the linearized operator governing the Oseen vortex is non-normal (Antkowiak & Brancher 2004). In a flow governed by a normal operator, the eigenvalue spectrum is sufficient to determine if all perturbations decay. However, in flows governed by non-normal (i.e. non-self-adjoint) operators the eigenvalue spectrum is inadequate. This is because the eigenfunctions of a non-normal operator are not mutually orthogonal; perturbations formed from superposition of non-orthogonal eigenfunctions can experience energy growth even when each constituent eigenfunction evolving in isolation undergoes monotonic decay. Such growth occurs for a finite period of time, before the inevitable decay sets in, and is algebraic, instead of exponential as in the case of normal modes. This phenomenon of temporary amplification is known as *transient growth*. Such growth may often be enough to cause transition to turbulence and as such has received considerable recent attention. (See Schmid & Henningson (2001) for an exposition of these results and a comprehensive review.) Transient growth analysis involves solution of the initial value problem for small-amplitude perturbations to a given base flow. To determine the perturbations that maximize energy growth, the linearized equations for perturbation quantities are solved, as in classical normal-mode stability theory. Unlike normal-mode analysis, however, no exponential-in-time behaviour of the perturbations is assumed.

While transient growth is a known mathematical phenomenon, its implications for hydrodynamic stability have only recently been realized (e.g. Farrell 1988; Trefethen *et al.* 1993). Over the past decade, numerous studies – spurred by the realization that several-orders-of-magnitude growth is possible even in stable flows – have addressed the transient growth characteristics of wall-bounded shear flows. The motivation has been to explain either the experimentally observed transition to turbulence at sub-critical Reynolds numbers (as in channel flow) or even the very growth of perturbations in flows that are determined to be unconditionally stable in terms of normal-mode analysis (e.g. pipe Poiseuille and plane Couette flows). ‘Bypass transition’ scenarios have been proposed (Butler & Farrell 1992; Reddy & Henningson 1993) in which transient growth elevates perturbations to levels where nonlinear effects become important, resulting in fully developed turbulence via subsequent instabilities of these nonlinear states. In addition to explaining transition in a stable flow, transient growth has been proposed as an ingredient of the turbulence regeneration/self-sustenance process in the turbulent boundary layer. Schoppa & Hussain (2002) have demonstrated that transient growth in the frequently occurring normal-mode stable near-wall streaks produces the streamwise vortices crucial for turbulence sustanence and transport phenomena in turbulent boundary layers.

The Oseen vortex is a representative analytical flow consisting of a vortical core surrounded by swirling potential flow and bears close analogies to plane shear flows with regard to stability. In particular, the flow is normal-mode stable and the linearized operator governing the evolution of small-amplitude perturbations is non-normal. Therefore it is natural to enquire if the vortex supports transient growth; and, if so, what orders of growth are possible. These questions motivate the present study. Whether the nonlinear evolution of growing perturbations results in transition and fully developed turbulence is an important question, but outside the scope of this paper.

In contrast to the case of plane shear flows, there has been little study of transient growth characteristics in vortex-dominated flows. Smith & Rosenbluth (1990) found that hollow vortex columns, whose vorticity peaks away from the axis, support a two-dimensional algebraic instability whose effect is to shift the vorticity peak to the axis. Transient growth of two-dimensional spiral-shaped perturbations has also been found in hurricane-like geophysical vortices maintained by radial inflow (Nolan & Farrell 1999). Montgomery & Kallenbach (1997) investigated the role of vortex Rossby waves in the axisymmetrization of perturbed two-dimensional vortices, and showed how outward-propagating spiral disturbances can cause vortex intensification. Similar spiral-shaped perturbations are found in the present work to lead to the growth of core perturbation energy.

Arendt, Fritts & Andreassen (1997) solved the initial value problem for three-dimensional core vorticity perturbations in a Rankine vortex (having a core with solid-body rotation, and potential velocity distribution outside). They found that an arbitrary perturbation evolves solely as the superposition of normal-mode solutions – the well-known Kelvin vortex waves (see e.g. Saffman 1992); i.e. the eigenmodes are complete for the class of perturbations contributing vorticity only within the core. All Kelvin-wave modes are neutrally stable, and no transient growth seems possible for perturbations obtained by superposing such modes. In contrast, the transient-growth modes revealed in the present study are capable of sustained and significant growth. Crouch (1997) and Fabre, Jacquin & Loof (2002) studied the evolution of two vortex dipoles in the context of the aircraft wake flow. Although this flow is normal-mode unstable, transient growth can nevertheless play an important role in accelerating vortex cross-linking and promoting circulation decay, thereby providing a possible means for alleviating the aircraft wake hazard. Transient growth in this flow, much like normal-mode instability, is reliant upon the strain induced on a vortex by adjacent vortices. This mechanism is hence absent in an isolated vortex.

Schmid *et al.* (1993) have studied the potential for transient growth in the q-vortex (a vortex with Gaussian axial velocity and axial vorticity profiles). While this flow has growing normal modes, Schmid *et al.* find that perturbations formed by superpositions of the stable eigenmodes are likely to cause large transient growth. The 'eigenvalue sensitivity' of the linearized operator was calculated to estimate the extent of transient growth; however, the growing transient perturbations were not obtained, nor were the physical mechanisms of growth investigated. (The eigenvalue sensitivity, i.e. how much the eigenvalues change when a linear operator is perturbed, provides an upper bound for transient amplification possible; see Trefethen (1992).) Transient growth in the Oseen vortex (having the same azimuthal velocity profile as the q-vortex), suggested by the results of Schmid *et al.* (1993), has been confirmed in the recent work of Antkowiak & Brancher (2004) (this simultaneous work has just come to our attention). They focus on the growth of bending waves (perturbation azimuthal wavenumber $m = \pm 1$) and discuss the growth mechanisms in the limit of two-dimensional perturbations. Our work involves the analysis of transient growth characteristics for other wavenumbers as well, with emphasis on the physical mechanisms responsible for transient growth and decay.

It should be noted that the framework of transient growth analysis is closely connected to that of rapid distortion theory (RDT): both approaches address the initial value problem for small-amplitude, arbitrary perturbations to a given flow. The RDT analysis of Miyazaki & Hunt (2000) shows that perturbations external to the vortex core experience algebraic growth. Thus the fact that transient growth is found in the Oseen vortex is not, in itself, surprising. The usefulness of the following analysis lies in its being able to determine the amplification levels possible, to extract the most 'dangerous' modes, and, thereby, to study the possible genesis and evolution of fully developed turbulence. In contrast, the framework of RDT is tuned to the statistical analysis of turbulence evolving from prescribed stochastic initial conditions. There is another important difference between prior RDT analysis and the present work. Miyazaki & Hunt modelled the vortex either as a solid rotating rod or as a deformable but impenetrable surface. Herein, we obtain the full perturbation velocity field, which allows the study of core fluctuation growth and should facilitate analysis of nonlinear perturbation evolution, possibly towards vortex transition.

In the following, we formulate the transient growth problem for an Oseen vortex to determine initial conditions capable of causing perturbation energy growth (§ 2). Next, we discuss the physical mechanisms of linear energy growth and decay (§ 3). Numerical results of growth characteristics are presented and discussed in § 4. Concluding remarks appear in § 5.

2. Problem formulation and numerics

We consider small-amplitude perturbations to an Oseen vortex column: $V = (1 - \exp(-r^2))/r$. We use cylindrical (r, θ, z) coordinates, with the corresponding velocity perturbation components (u, v, w) (figure 1a). Upper-case quantities (V, Ω) denote the base flow. The perturbation is Fourier-decomposed along θ and z:

$$\{u, v, w, p\}(r, \theta, z, t) = \mathrm{Re}[\{\mathrm{i}\widetilde{u}, \widetilde{v}, \widetilde{w}, \widetilde{p}\}(r, t)\exp(\mathrm{i}m\theta + \mathrm{i}kz)]. \qquad (2.1)$$

Since two eigenmodes with unequal azimuthal or axial wavenumbers (m or k) are necessarily orthogonal, no transient growth is possible through superposition of such modes. The transient growth problem is thus parameterized by the wavenumbers

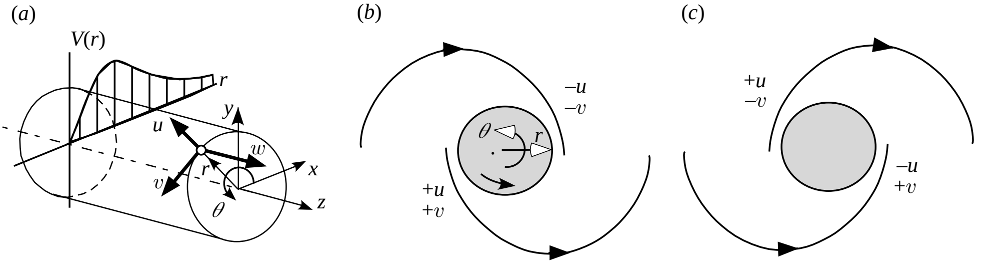

FIGURE 1. (*a*) Schematic of mean flow and coordinate systems used. Schematics of streamlines: (*b*) 'positive-tilt', producing positive uv for energy growth; (*c*) 'negative-tilt', producing negative uv for decay.

(m, k). We insert the perturbation form (2.1) into the Navier–Stokes and continuity equations and linearize the problem. After eliminating pressure, the system of equations can be expressed in the form

$$\frac{\mathrm{d}}{\mathrm{d}t}\mathscr{M}\widetilde{\boldsymbol{u}} = (-\mathrm{i}\mathscr{L} + \nu\mathscr{V})\,\widetilde{\boldsymbol{u}}, \tag{2.2}$$

where the matrix operators are

$$\mathscr{M} = \begin{pmatrix} 1 & 0 & \dfrac{1}{k}\dfrac{\mathrm{d}}{\mathrm{d}r} \\ 0 & 1 & -\dfrac{m}{kr} \\ 0 & 0 & 0 \end{pmatrix}, \quad \mathscr{L} = \begin{pmatrix} \beta & \dfrac{2V}{r} & \dfrac{\beta}{k}\dfrac{\mathrm{d}}{\mathrm{d}r} + \dfrac{\beta'}{k} \\ \mathscr{D}V & \beta & -\dfrac{\beta m}{kr} \\ \mathscr{D} & \dfrac{m}{r} & k \end{pmatrix}, \tag{2.3a}$$

and

$$\mathscr{V} = \begin{pmatrix} \mathscr{D}' - \eta & -\dfrac{2m}{r^2} & \dfrac{1}{k}\left[\mathscr{D}'\dfrac{\mathrm{d}}{\mathrm{d}r} - \eta\dfrac{\mathrm{d}}{\mathrm{d}r} + \dfrac{2m^2}{r^3}\right] \\ -\dfrac{2m}{r^2} & \mathscr{D}' - \eta & -\dfrac{m}{kr}\left[\mathscr{D}\dfrac{\mathrm{d}}{\mathrm{d}r} - \eta\right] \\ 0 & 0 & 0 \end{pmatrix}. \tag{2.3b}$$

Here ν is the kinematic viscosity, $\beta = mV/r$, $\eta = m^2/r^2 + k^2$, $\mathscr{D} = \mathrm{d}(\cdot)/\mathrm{d}r + (\cdot)/r$ and $(\cdot)' \equiv \mathrm{d}(\cdot)/\mathrm{d}r$. The boundary conditions (e.g. Ash & Khorrami 1995) are that the perturbation decays to zero as $r \rightarrow \infty$ and that at the vortex axis

$$\left.\begin{array}{ll} \widetilde{u}, \widetilde{v}, \widetilde{w}' = 0, \quad \text{when } m = 0 \quad \text{(axisymmetric modes)}, \\ \widetilde{u}', \widetilde{u} + m\widetilde{v}, \widetilde{w} = 0, \quad \text{when } m = \pm 1 \quad \text{(helical bending wave modes)}, \\ \widetilde{u}, \widetilde{v}, \widetilde{w} = 0, \quad \text{when } |m| > 1. \end{array}\right\} \tag{2.4}$$

The volume-integrated perturbation energy is

$$E(t) = \frac{1}{2}\int_{z=0}^{2\pi/k}\int_{\theta=0}^{2\pi}\int_{r=0}^{\infty}\left(u^2 + v^2 + w^2\right)\, r\,\mathrm{d}r\,\mathrm{d}\theta\,\mathrm{d}z \equiv (\boldsymbol{u}, \boldsymbol{u}), \tag{2.5}$$

where $\boldsymbol{u} = (u, v, w)$ and $(\cdot, \cdot)$ denotes inner product. The goal of our linear analysis is to determine 'optimal perturbations' (see § 4) that maximize the energy amplification $E(t)/E(0)$ at time t. This optimization problem is solved following the approach of Corbett & Bottaro (2000), briefly summarized below.

Given an initial condition $\tilde{\boldsymbol{u}}(0)$ the perturbation at a subsequent time τ can be represented as $\tilde{\boldsymbol{u}}(\tau)=\mathscr{P}(\tau)\tilde{\boldsymbol{u}}(0)$, where $\mathscr{P}$ is the propagation operator implicit in (2.2). Then, the energy amplification can be written as

$$\frac{E(\tau)}{E(0)}=\frac{(\mathscr{P}\tilde{\boldsymbol{u}}(0),\mathscr{P}\tilde{\boldsymbol{u}}(0))}{(\tilde{\boldsymbol{u}}(0),\tilde{\boldsymbol{u}}(0))}=\frac{(\tilde{\boldsymbol{u}}(0),\mathscr{P}^{+}\mathscr{P}\tilde{\boldsymbol{u}}(0))}{(\tilde{\boldsymbol{u}}(0),\tilde{\boldsymbol{u}}(0))}. \tag{2.6}$$

Here '+' denotes the adjoint operator. The final form in (2.6) is the Rayleigh quotient, whose maximum value equals the largest eigenvalue of $\mathscr{P}^{+}\mathscr{P}$, this value being attained when $\tilde{\boldsymbol{u}}$ coincides with the corresponding eigenvector. Note that $\mathscr{P}^{+}\mathscr{P}$ is self-adjoint and positive definite, so that all its eigenvalues are real and positive. The largest possible energy amplification at time t, denoted as the *gain* $G(t)$, is thus determined by solving the eigenvalue problem for $\mathscr{P}^{+}\mathscr{P}$. The adjoint problem needed here is derived through integration by parts of (2.2), using the inner product defined in (2.5). The largest eigenvalue is calculated using the technique of power iteration, involving repetitive forward-in-time integrations of the direct problem and backward-in-time integrations of the adjoint problem. See Corbett & Bottaro (2000) for details.

Numerical solution of the transient growth problem involves the spatial and temporal discretization of the governing direct and adjoint equations. Spatial discretization is achieved here through a standard Chebyshev spectral collocation method (Canuto *et al.* 1988). While the radial domain is, in principle, semi-infinite, truncating the domain at a large finite value R was found to be adequate. The radial coordinate $r \in [0, R]$ is mapped to a computational coordinate $\xi \in [-1, 1]$ as $\xi = 2r/R - 1$. Domain-size independence of the solutions was checked by varying R; most of the results herein were obtained with $R = 15$ and $N = 150$, where N is the number of Chebyshev polynomials used. Temporal discretization is implemented using the first-order backward Euler method, which is unconditionally stable for both the direct and adjoint problem integrations. A golden search algorithm was used for determining the maxima of $G(t; m, k, Re)$; here Re is the vortex Reynolds number, defined as circulation/viscosity.

The numerical codes used here were validated in three stages. First, discretization of the operators appearing in (2.2) was checked by assuming exponential-in-time perturbations and solving the resulting generalized eigenvalue problem. The base flow was modified by superposing a jet-like or wake-like axial velocity profile. The eigenvalues obtained for this 'q-vortex' agreed to at least five significant digits with the results of Mayer & Powell (1992). The axial velocity term was set to zero, to recover the Oseen vortex, for the transient growth analysis presented herein. Second, the adjoint-problem numerics were validated by ensuring that the biorthogonality condition between the eigenmodes of the direct and adjoint problems was satisfied to within numerical precision. Finally, the time-stepping procedure was verified by comparing energy evolutions obtained from linear analysis with those from direct numerical simulation (DNS) of the linearized Navier–Stokes equation, using the same initial three-dimensional perturbation vorticity field (see figure 11*a*, discussed in § 4). Validation of the DNS code, implementing the method of Rennich & Lele (1997), and the usefulness of this algorithm for simulating an isolated vortex have been discussed in Pradeep & Hussain (2004).

3. Inviscid mechanisms of growth and its arrest

Before proceeding to the numerical results, it is useful to examine the (linear and inviscid) mechanisms of perturbation growth and decay. Perturbation dynamics are analysed by considering the Reynolds stress uv, which governs energy evolution. The inviscid perturbation energy equation is

$$\frac{\partial}{\partial t}e+\frac{V}{r}\frac{\partial}{\partial \theta}e=-\frac{1}{r}\frac{\partial}{\partial r}(rup)-\frac{1}{r}\frac{\partial}{\partial \theta}(pv)-\frac{\partial}{\partial z}(pw)-uv\,r\frac{\partial}{\partial r}\frac{V}{r}, \tag{3.1}$$

where $e=\frac{1}{2}(u^2+v^2+w^2)$. Upon volume-integration, the advection and pressure-work terms drop out, yielding

$$\mathrm{d}E/\mathrm{d}t=-\int uv\,r(V/r)'\,\mathrm{d}V, \tag{3.2}$$

wherein the production term, $-uv\ r(V/r)'$, shows that positive Reynolds stress $uv>0$ is necessary for energy growth. (Note that the sign on the Reynolds stress uv is opposite to that typical in plane shear flows since in the present case the mean velocity gradient is negative. Thus uv has to be positive for $\mathrm{d}E/\mathrm{d}t>0$.)

There are two distinct mechanisms of perturbation energy evolution at play. The first, purely two-dimensional, involves differential azimuthal advection of the perturbation axial vorticity. Such advection leads to the eventual decay of initially growing perturbations. The second mechanism is three-dimensional and involves tilting of vortex lines from the radial towards the azimuthal direction and concomitant vortex stretching. These mechanisms, discussed here in simplified inviscid flows, act in conjunction to govern the evolutions of the transient growth modes obtained through analysis (§ 4).

3.1. *Two-dimensional mechanism of growth arrest*

To understand the first mechanism, let us consider a two-dimensional perturbation ($k=0$ and $w=0$). Additionally, if the perturbation is axisymmetric ($m=0$), no growth is possible, because then u must vanish everywhere (by continuity), and hence no Reynolds stress can be generated. The structure that a growing non-axisymmetric ($m\neq 0$) perturbation must have is clarified by considering the perturbation streamfunction ψ, with $u=\partial\psi/r\partial\theta$ and $v=-\partial\psi/\partial r$. We can distinguish two types of streamlines: ‘positive-tilt’ streamlines are those along which r increases as θ increases, contributing co-gradient Reynolds stress, i.e. positive uv (figure 1*b*); contrarily, ‘negative-tilt’ streamlines, along which r decreases as θ increases, contribute counter-gradient Reynolds stress, i.e. negative uv (figure 1*c*). An initial perturbation with predominantly positive-tilt streamlines will thus experience energy growth. This growth, however, is temporary since the mean flow transforms a perturbation with positive-tilt streamlines into one with negative-tilt streamlines. The rate at which this transformation occurs (hence the period of growth) depends on the mean strain rate $r(V/r)'$ and hence decreases with increasing radius. Note that perturbations located farther away from the axis experience growth for a longer duration than those closer to the axis (see § 4.3).

The following will show that the effects of mean strain and vorticity are counteractive to each other’s role in energy growth. Whereas mean strain is necessary for production (see 3.2), mean vorticity promotes vortex waves that dampen growth (see later). To isolate the two-dimensional mechanism we therefore consider a flow with only mean strain, namely flow outside a solid rotating rod. The velocity field is $V\sim 1/r$, which approximates the potential region of the Oseen vortex. Choice of the

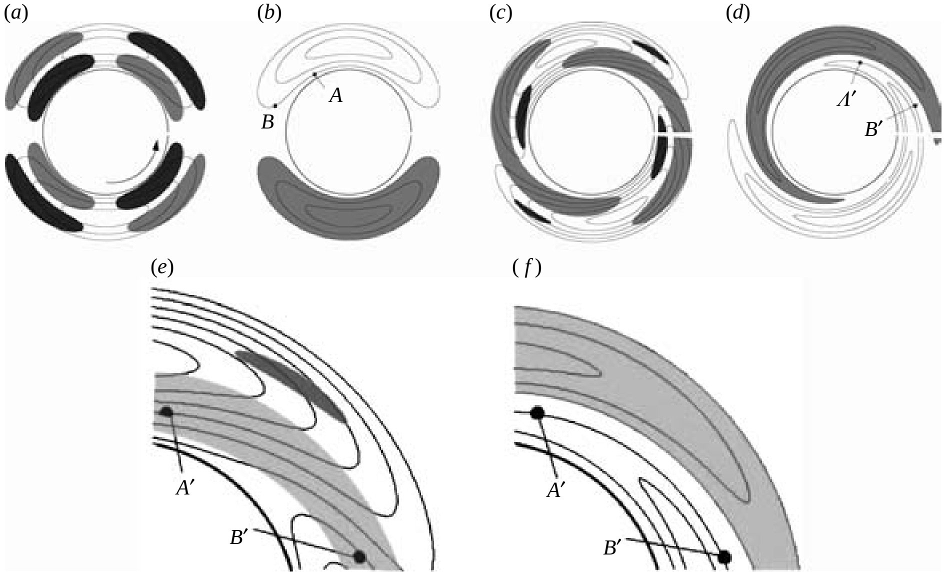

FIGURE 2. Contours of ψ (a,c) and ω (b,d) at $t=0$ (a,b) and $t=100$ (c,d) illustrating the two-dimensional mechanism of transient growth cessation. Light-shaded regions in (a,c) denote $uv<0$ and dark-shaded regions $uv>0$. Shaded regions in (b,d) denote negative ω. Two fluid particles initially at A, B are advected to A', B', respectively, at $t=100$. Close-up views of ψ contours (e) and ω contours (f) at $t=100$.

rod eliminates the numerical complication of singularity at the vortex axis, and also the deflection of the axis, as in the case of bending waves. We consider the simplest non-axisymmetric mode, $m=1$ (the bending wave), with the analytical perturbation,

$$\psi(r,\theta,t=0) = \mathrm{Re}\{\widetilde{\psi}(r,0)\exp(\mathrm{i}\theta)\}, \quad \widetilde{\psi} = J_1(r),$$

where J_1 is the Bessel function of order one. The rod radius is set to $r_0=3.8317$, the first zero of J_1, so that the impenetrability condition at the solid surface is satisfied. The associated axial vorticity perturbation, $\omega=-\nabla^2\psi$, is then given by $\widetilde{\omega}=J_1(r)$. The governing equation for perturbation vorticity (for zero-mean-vorticity flow) reduces to $\partial_t\widetilde{\omega}=-\mathrm{i}\widetilde{\omega}/r^2$, and has the solution $\widetilde{\omega}(r,t)=\widetilde{\omega}(r,0)\exp(-\mathrm{i}t/r^2)$. Streamfunction evolution is then given by

$$\widetilde{\psi}(r,t) = \left(\frac{1}{2}\int^{r} \widetilde{\omega}(r',t)r'^{2}\,\mathrm{d}r'\right)r^{-1} - \left(\frac{1}{2}\int^{r} \widetilde{\omega}(r',t)\,\mathrm{d}r'\right)r.$$

These ψ and ω fields are shown at $t=0$ and $t=100$ (i.e. after approximately half a turnover time) in figure 2. Initially, there is a symmetric distribution of $uv>0$ and $uv=0$ (figure 2a) in an axisymmetric mean strain field, and hence zero net production. Consider two fluid particles, initially at locations A and B (figure 2b), that have equal ω. The particle A, lying at a smaller radius than B, is advected with greater angular velocity by the mean swirl. At $t=100$, the fluid particles, now denoted A' and B', occupy positions as shown in figures 2(d). Since ω is materially conserved in this inviscid flow, A and B always lie on the same ω-contour (figure 2f). Differential advection thus leads to a progressively tightening spiral pattern of ω contours (figure 2d).

Within the spiral pattern, the layers become progressively thinner (see, for example, figures 15*c*, 17*k*), so that the curvature progressively becomes less important and the radially separated layers can then be treated as a plane shear flow (where ψ and ω contours coincide). (Such an idealization to a plane shear flow of parallel sheets of vorticity is effective in explaining why perturbation growth in this inviscid flow cannot be indefinite and is arrested by the transformation of streamlines from positive tilt to negative tilt.) Hence, the pattern of ω and ψ contours, coincident by construction at $t=0$, will continue to spiral in a similar fashion at subsequent times (compare figures 2*c* and 2*d*). This implies that a region of positive-tilt streamlines (i.e. spiralling outward with increasing θ) will be transformed to a region of negative-tilt streamlines: compare the streamline segment connecting A and B (when they were on the same streamline) to streamlines in the vicinity of A' and B' (when they are on different streamlines; see figure 2*e*). Note that A' and B' are both now in a region of negative uv (figure 2*e*). Differential advection thus leads to a progressive dimunition of total positive uv. As a result, the integrated positive production contributing to three-dimensional energy growth is reduced and the perturbation decays. We thus see a generic mechanism of inviscid arrest of growth by mean swirl. This mechanism of transient growth arrest through the differential advection of ω_z by the mean swirl, resulting in the deformation of ω_z contours and transformation of streamlines from positive tilt to negative tilt, will hereafter be called the *shearing mechanism*. A similar mechanism of transient growth is known in plane shear flows (Farrell 1988).

3.2. *Three-dimensional mechanism*

We now turn to the second growth mechanism, involving a three-dimensional perturbation. Consider an axisymmetric ($m=0$) perturbation, for which the two-dimensional vorticity shearing mechanism is absent. The inviscid governing equations (2.2) can be written as a coupled system for perturbation velocity amplitudes $\widetilde{u}$ and $\widetilde{v}$:

$$\mathrm{i}\frac{\mathrm{d}}{\mathrm{d}t}\left(\widetilde{u}-\frac{1}{k^2}\mathscr{D}'\widetilde{u}\right)=\frac{2V}{r}\widetilde{v},\quad \mathrm{i}\frac{\mathrm{d}}{\mathrm{d}t}\widetilde{v}=\widetilde{u}\mathscr{D}V=\widetilde{u}\left(\frac{\mathrm{d}V}{\mathrm{d}r}+\frac{V}{r}\right). \tag{3.3}$$

We consider a model mean flow in which pure straining (potential vortex) and vortical (solid-body rotation) flows are superposed:

$$V=\alpha/r+\beta r/2. \tag{3.4}$$

With $\beta=0$, the mean flow corresponds to a potential vortex, whose vorticity $\mathscr{D}V$ is zero everywhere, except on the axis. With $\alpha=0$, the mean flow is vortical, with zero strain rate everywhere.

3.2.1. *Pure straining flow*

For potential flow ($\beta=0$) the coupling term in the $\widetilde{v}$ equation in (3.3) disappears. Thus, any initial azimuthal velocity perturbation remains steady, while the evolution of $\widetilde{u}$ is driven by $\widetilde{v}$. The $\widetilde{u}$ solution then is

$$\widetilde{u}(r,t)=\alpha t\,[F_1+F_2]+\widetilde{u}(r,0), \tag{3.5}$$

where

$$F_1=2\mathrm{i}k\left(\int^r\frac{1}{r'}\widetilde{v}K_1(kr')\,\mathrm{d}r'\right)I_1(kr),$$

$$F_2=-2\mathrm{i}k\left(\int^r\frac{1}{r'}\widetilde{v}I_1(kr')\,\mathrm{d}r'\right)K_1(kr).$$

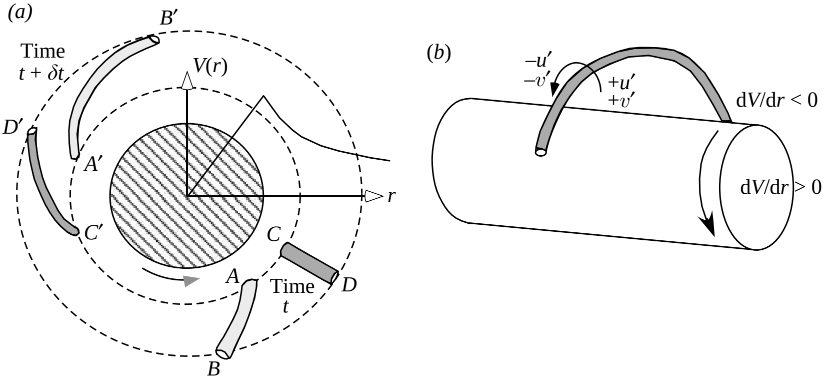

FIGURE 3. (*a*) Illustration of vortex filament stretching by mean swirl. Material points A, B are differentially advected to A', B' and points C, D to C', D', resulting in lengthening of the filaments, hence producing enstrophy. (*b*) Illustration of positive-uv generation by an azimuthal filament wrapping around a vortex column.

I_1 and K_1 are modified Bessel functions of order one. Thus, any initial $\widetilde{v}$ perturbation generates linear-in-time growth of $\widetilde{u}$ (and thence also of $\widetilde{w}$, through the continuity equation). Consequently, there is quadratic-in-time perturbation energy growth, with energy becoming unbounded with time. It should be noted that a similar result is obtained from rapid distortion theory (see Miyazaki & Hunt 2000).

The coupling term in the $\widetilde{u}$ equation (3.3) corresponds physically to the tilting and stretching of radial vorticity by the mean strain, resulting in the generation of azimuthal vorticity. To see this consider the perturbation vorticity equations:

$$\frac{\partial \omega_r}{\partial t} + \frac{V}{r}\frac{\partial \omega_r}{\partial \theta} = \Omega \frac{\partial u}{\partial z}, \tag{3.6}$$

$$\frac{\partial \omega_\theta}{\partial t} + \frac{V}{r}\left(\frac{\partial \omega_\theta}{\partial \theta} + \omega_r\right) = \omega_r \frac{\partial V}{\partial r} + \Omega \frac{\partial v}{\partial z}, \tag{3.7}$$

$$\frac{\partial \omega_z}{\partial t} + \frac{V}{r}\frac{\partial \omega_z}{\partial \theta} + u\frac{d\Omega}{dr} = \Omega \frac{\partial w}{\partial z}, \tag{3.8}$$

where $\Omega = \mathscr{D}V$ is the mean vorticity. For the case of zero mean vorticity and axisymmetric perturbation, the equations reduce to

$$\frac{\partial \widetilde{\omega}_r}{\partial t} = 0, \quad \frac{\partial \widetilde{\omega}_\theta}{\partial t} = \widetilde{\omega}_r\, r\frac{\partial}{\partial r}\left(\frac{V}{r}\right), \quad \frac{\partial \widetilde{\omega}_z}{\partial t} = 0. \tag{3.9}$$

Thus, the mean strain field generates and amplifies $\widetilde{\omega}_\theta$ whenever $\widetilde{\omega}_r$ is non-zero. Since in an axisymmetric flow, $\widetilde{\omega}_r$ results only from axial variation of $\widetilde{v}$, and growing $\widetilde{\omega}_\theta$ implies growth of $\widetilde{u}$ and $\widetilde{w}$, perturbation growth in (3.5) is via this vortex stretching mechanism, associated with the differential azimuthal advection of a vortex filament, as illustrated in figure 3(*a*). Azimuthally aligned vortex filaments generate $uv > 0$ by the transport of mean azimuthal momentum V, as illustrated in figure 3(*b*). Hence the growth of perturbation energy.

3.2.2. *Solid-body rotation*

In the case of solid-body rotation ($\alpha = 0$, $\beta \neq 0$), on the other hand, $\widetilde{u}$ and $\widetilde{v}$ evolutions, described by (3.3), are mutually coupled. Although having no production (the strain rate is zero), the solid-body rotation (vortical) case helps explain perturbation

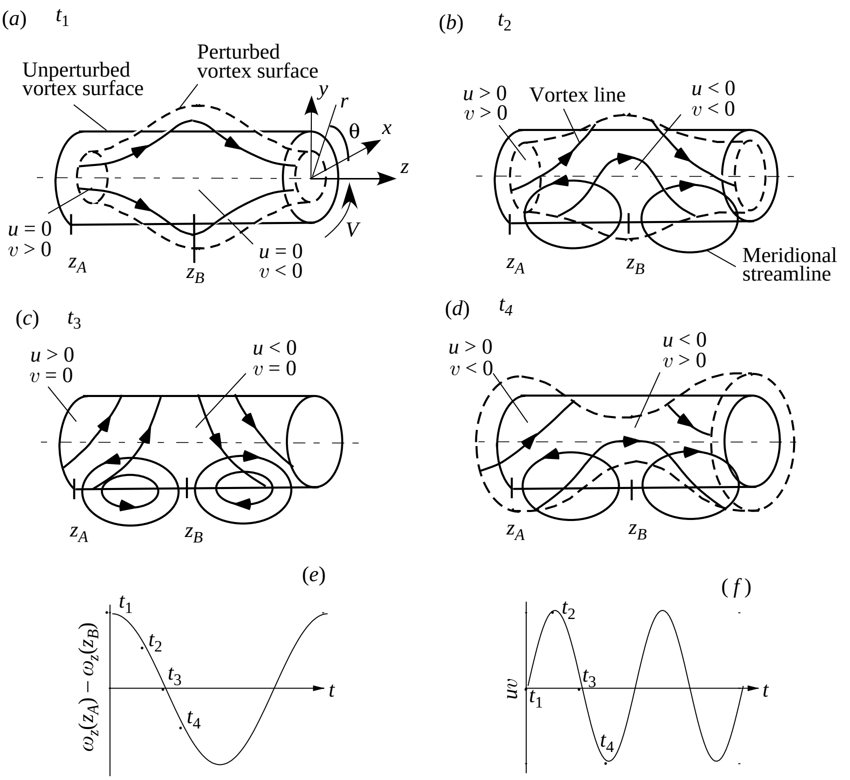

FIGURE 4. Schematic of four stages (*a–d*) of CD oscillation at four successive instants t_1–t_4 on a vortex column for one wavelength of CD. Streamlines in the meridional plane (r, z) also shown. t_1–t_4 are identified in: (*e*) the time variation of axial vorticity perturbation ω_z; and (*f*) time variation of volume-integrated Reynolds stress uv. Note that the latter oscillates at twice the frequency of ω_z.

evolution in the vorticity-dominated region (i.e. the core) of the Oseen vortex. The mutual coupling between $\tilde{u}$ and $\tilde{v}$ causes an initial $\tilde{v}$ perturbation to generate $\tilde{u}$, which, in turn, diminishes the magnitude of the $\tilde{v}$ perturbation.

The resulting oscillatory motion (*core dynamics*, CD) has been discussed in Melander & Hussain (1994). Here we review the CD mechanism with emphasis on the evolution of uv. Consider a cylindrical vortex column with a perturbed, sinusoidal variation of core area (figure 4*a*). Initially, at $t = t_1$, the perturbation contains only ω_r, ω_z and v – all other vorticity and velocity components being zero. Figure 4(*b–d*) shows three subsequent CD oscillation times t_2, t_3 and t_4. In each panel, the solid line denotes the unperturbed vortex surface, and the dashed line denotes the perturbed vortex surface. Two vortex lines on the perturbed vortex surface are shown at each stage. The instants t_1–t_4 are marked on the time-variation of perturbation vorticity (figure 4*e*) and of the Reynolds stress (figure 4*f*).

We discuss the dynamics in the vicinity of two axial planes, z_A and z_B (figure 4*a*), separated by half the perturbation axial wavelength. Since the perturbed vortex surface encloses constant circulation $\Gamma = 2\pi r(V + v)$ at each cross-section, the perturbation azimuthal velocity $v > 0$ on the vortex surface at z_A and $v < 0$ at z_B (at t_1). The perturbation radial velocity u is zero everywhere in the flow, since the vortex lines are uncoiled ($\omega_\theta = 0$). Thus the Reynolds stress is also zero (figure 4*f*). Because of the differential swirl along the vortex surface, the vortex lines immediately begin coiling (starting at t_1), so as to generate ω_θ and meridional flow (u and w) of the form shown in figure 4(b), at t_2. The meridional flow contributes $u > 0$ near z_A and $u = 0$ near z_B at this stage of the oscillation (at t_2); thus $uv > 0$ everywhere along the column (figure 4b). Axial vorticity stretching (compression) by the meridional flow near z_B (z_A) tends to reduce the vortex-core area variation. Thus, ω_r is decreased. Subsequently, at t_3, the vortex surface returns to its unperturbed shape (figure 4c), when there is non-zero u, but zero v. That is, the Reynolds stress uv increases from zero, attains a maximum, and then decreases back to zero during the period t_1–t_3 (figure 4f). At t_3, while the vortex surface is instantaneously cylindrical, the vortex lines are maximally coiled, with maximal meridional flow. The vortex stretching/compression action of the induced meridional flow then causes the vortex-core area variation to reverse from that at t_1: core area is maximum at z_A and minimum at z_B (figure 4d). This reversal implies that now $v < 0$ at z_A and $v > 0$ at z_B; hence $uv = 0$ is generated. Note that the evolution from t_1 to t_3 comprises one quarter of the CD oscillation cycle (figure 4e). Thus, the wave motion, i.e. CD, is a simple consequence of coiling and uncoiling of vortex lines and would continue indefinitely in inviscid flow, but be damped in viscous flow.

The effect of mean vorticity is to cause any perturbation to evolve as a superposition of waves (such as CD), as shown by Arendt *et al.* (1997). Because of dispersion, various wave modes that interfere destructively at one instant will interfere constructively some time later. The resulting Reynolds stress, hence production, will undergo periodic oscillation, as also the perturbation energy. (An example of oscillatory energy evolution resulting from wave dispersion is given later in § 4.1; see figure 10.) This contrasts with pure straining motion, which produces unbounded growth in inviscid flow. Viscosity will cause damped oscillation in the vortical case and limit energy amplification in the pure straining case, with eventual perturbation energy decay in both.

3.2.3. *Roles of vorticity and strain*

The simultaneous effects of vorticity and strain can be assessed by numerically time-integrating (3.3). The initial perturbation is taken to be $\widetilde{v} = r^2 \exp(-(r - r_0)^2)$, with $\widetilde{u} = \widetilde{w} = 0$ (see initial $\widetilde{u}$, $\widetilde{v}$ profiles in figure 5). The associated vorticity field has only ω_r and ω_z, and the perturbation experiences growth via the vortex tilting/stretching mechanism.

Figure 5 plots the computed results for (a) volume-integrated perturbation energy, $E = \frac{1}{2}\int(u^2 + v^2 + w^2)\,\mathrm{d}V$; ($b$) $u(r)$ profile; (c) $v(r)$ profile; and (d) $uv(r)$ profile. Figure 5(b–d) depicts two cases of mean flow: $\beta = 0.1$ and 0.2, both for $\alpha = 1$. The quadratic energy growth in the pure straining (zero vorticity) case is arrested by the effects of vorticity ($\beta \neq 0$) (figure 5a), as discussed in the following.

We focus on the $\alpha \neq 0$, $\beta \neq 0$ dynamics and first discuss the $\beta = 0.1$ case. Early ($t \leqslant 4$) energy growth is nearly the same as for $\beta = 0$: because $\widetilde{u}$ is small its effect on $\widetilde{v}$ evolution is indeed insignificant; thus (3.5) is approximately valid. During this time, $\widetilde{u}$ grows rapidly from zero (figure 5b) due to the meridional flow induced by coiled vortex lines (as in figure 4b), while $\widetilde{v}$ (figure 5c) decays slowly. Hence, large $uv > 0$ is generated (figure 5d) due to the presence of both meridional flow and core area variation (figure 4b). Once $\widetilde{u}$ attains a sufficiently large amplitude, the coupling term in the $\widetilde{v}$ equation (3.3) becomes significant. The feedback effect of $\widetilde{u}$ is to progressively diminish $\widetilde{v}$ (figure 5c, at $t = 4, 8$ for $\beta = 0.1$). The decay of $\widetilde{v}$ is due to the tendency of the meridional flow (i.e. $\widetilde{u}$ and $\widetilde{w}$) to reduce the vortex-core area

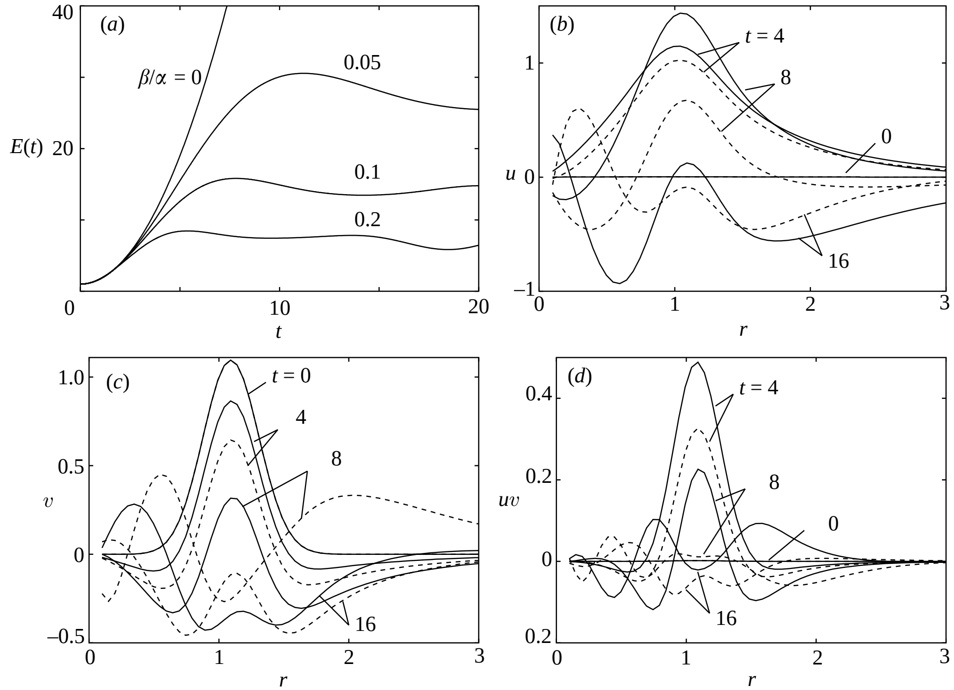

FIGURE 5. (a) Perturbation energy evolution for various cases of model flow (3.4). (b) Evolution of radial velocity perturbation $u(r)$. (c) Evolution of azimuthal velocity perturbation $v(r)$. (d) Evolution of $uv(r)$. In (b–d), solid lines are for $\beta = 0.1$ and dashed lines $\beta = 0.2$. In all cases $\alpha = 1$.

variation – as in figure 4(a,b) – inherent in the initial perturbation. This decay of $\widetilde{v}$, in turn, causes the rate of growth of the radial velocity perturbation also to diminish: compare the change in $\widetilde{u}$ amplitudes between $0 < t < 4$ and $4 < t < 8$ in figure 5(b). The magnitude of positive uv is reduced (figure 5d, at $t = 8$) because of the decay of $\widetilde{v}$, and perturbation energy growth is decreased (figure 5a). The persisting meridional flow then causes the initial core area variation to be reversed (as in figure 4d), implying that the sign of the $\widetilde{v}$ perturbation is also reversed (figure 5c, at $t = 16$) from that at $t = 0$. Subsequent evolutions of $\widetilde{v}$, $\widetilde{u}$ and $\widetilde{uv}$ resemble qualitatively the oscillatory behaviour in figure 4. The dominance of wave-like motions is also reflected in the oscillatory behaviour of $E(t)$ for $t > 5$ (figure 5a).

To re-emphasize, the maximum variation of the core diameter coincides with the minimum of meridional flow (figure 4a) and vice versa (figure 4d), explaining why $u(r)$ and $v(r)$ peak at different times (about 90° out of phase), and hence the evolution of $uv(r)$.

With increasing β/α, the mutual coupling between $\widetilde{v}$ and $\widetilde{u}$ is strengthened, and energy growth is arrested more rapidly (figure 5a). The amplification of $\widetilde{u}$ for $\beta/\alpha = 0.2$ is smaller than that for $\beta/\alpha = 0.1$ and also occurs over a shorter period of time, due to the strengthened coupling between $\widetilde{u}$ and $\widetilde{v}$.

3.2.4. *Inviscid arrest of growth*

The growth arrest seen in figure 5(a) can be understood in terms of perturbation vorticity evolution. It can be seen from (3.7) that the presence of radial vorticity ω_r leads to the growth of azimuthal vorticity ω_θ, through the stretching of spiral vortex

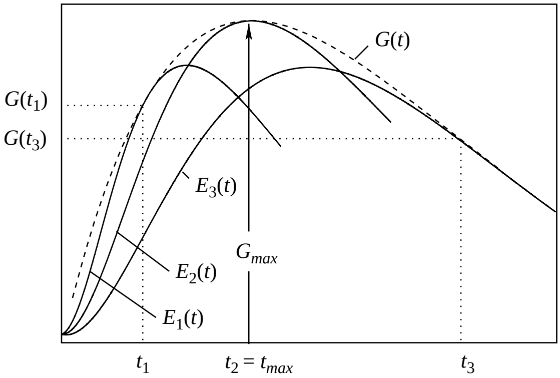

FIGURE 6. Definition sketch of various terms used in transient growth analysis. $G(t)$ is the gain curve – enveloping all energy growth curves $E(t)$ – its maximum value G_{max} occurring at $t=t_2=t_{max}$. $E_1(t)$–$E_3(t)$ are the energy evolutions of three different optimal perturbations. $E_1(t)$, $E_3(t)$ are the $t=t_1, t_3$ optimals, whereas $E_2(t)$ is the global optimal.

filaments, and hence coiling of vortex lines (figure 3*a*). In pure straining flow, ω_r remains unchanged, and there is continual growth of ω_θ. The radial motions induced by ω_θ generate positive uv, causing energy growth, which is unbounded. The effect of mean vorticity is to deplete radial vorticity ω_r by causing radially aligned vortex lines to be oriented into the azimuthal direction, by vortex line coiling (figure 4*b*). Meridional motions (u and w) induced by coiled vortex lines decrease the core area variation (figure 4*c*), reducing v and hence also the Reynolds stress uv. The stress is eventually reduced to zero, arresting production and energy growth. Since vortex line coiling is the result of differential swirl along the vortex core, the rate of coiling (hence the rate of depletion of ω_r) increases with increasing mean vorticity. Therefore, growth arrest occurs more rapidly with increasing β/α, i.e. with increasing vorticity.

In summary, this simple model flow illustrates the counteractive roles of mean vorticity and strain: *whereas strain causes transient growth, vorticity acts to promote wave motions that lead to the arrest of transient growth.* The effect of the radial inhomogeneity of the strain-to-vorticity ratio is to select a preferred radial location of the optimal perturbations, as discussed later for the case of the Oseen vortex.

4. Optimal perturbations

The primary quantity obtained by solving the transient growth problem is the gain function $G(t)$, which is the envelope of perturbation energy evolution curves $E(t)$ (figure 6). The maximum value of $G(t)$, denoted as G_{max}, is attained at $t=t_{max}$. A perturbation whose $E(t)$ touches $G(t)$ at $t=\tau$ is termed the '$t=\tau$ optimal'. The perturbation is optimal in the sense that no other perturbation achieves greater energy amplification at $t=\tau$. The perturbation attaining the amplification G_{max} at $t=t_{max}$ is termed the *global optimal*. Different initial perturbations having different evolutions $E(t)$ are optimal at different times. Note that a $t=\tau$ optimal may continue to amplify beyond the time τ (e.g. curve $E_1(t)$ in figure 6), and that a single perturbation may be optimal not just for one particular amplification time τ, but for a range of amplification times (e.g. curve $E_3(t)$ coincides with $G(t)$ for $t > t_3$).

It is important to investigate not only the global optimal (for each given m, k, and Re), but also the $t=\tau$ optimals experiencing lesser growth. This is because the global optimals may grow too slowly (hence get overwhelmed by lesser, but faster,

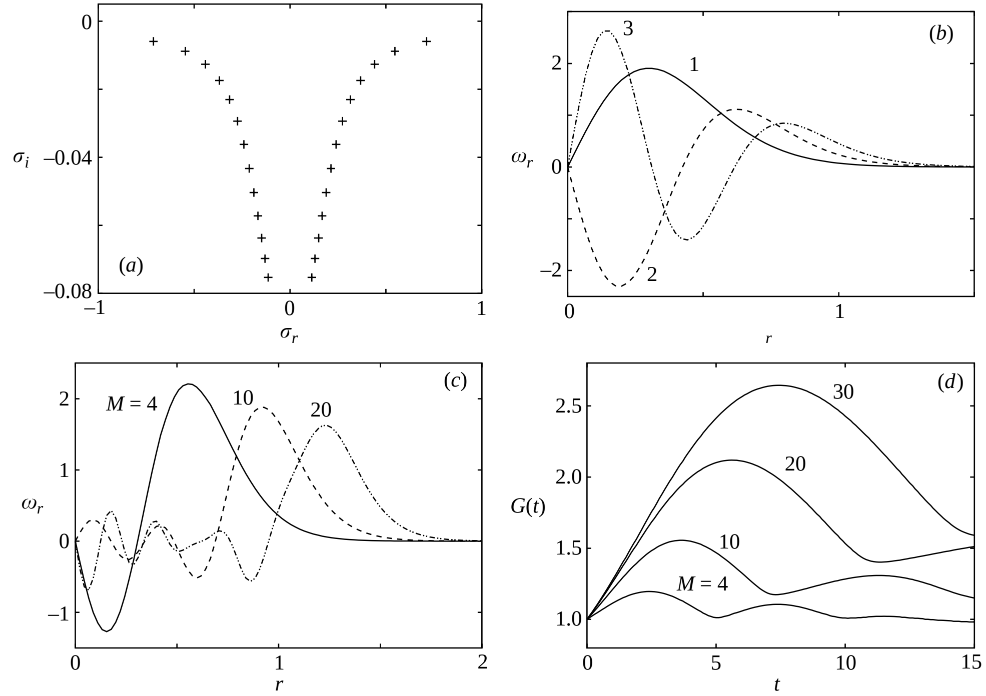

FIGURE 7. Results from eigenvalue-based transient growth analysis for an Oseen vortex. (*a*) The eigenvalue spectrum σ_i vs. σ_r. (*b*) ω_r profiles of the first three modes. (*c*) Variation of optimal mode ω_r profiles with M; the modes are the global optimals with G_{max} corresponding to peak values of G in (*d*). (*d*) Variation of $G(t)$ with M. In all cases, $m=0$, $k=2$ and $Re=10^4$.

growing perturbations). It will be seen in the following that this is indeed the case for axisymmetric modes.

In the following, we discuss results obtained by transient growth analysis, focusing on the evolutionary dynamics for the two simplest cases, namely axisymmetric ($m=0$) (§4.2) and bending wave ($|m|=1$) modes (§4.3). But before proceeding to these results, we consider in §4.1 transient growth modes synthesized by superposing a few eigenmodes of the Oseen vortex, all individually decaying. Such analysis provides physical insights into the transient growth mechanisms in the vortex flow.

4.1. *Eigenfunction-based analysis*

Transient growth in a normal-mode-stable flow is possible only when the governing linearized operator is non-normal, i.e. the operator does not commute with its adjoint, and, hence, the eigenmodes are not mutually orthogonal. Then, perturbations obtained by superposition of decaying eigenmodes can experience temporary growth (see e.g. Schmid & Henningson 2001).

The Oseen vortex features a multiplicity of eigenmodes for each specific value of the wavenumber pair (m,k). The eigenmodes are obtained by considering perturbations of the form

$$\{u, v, w, p\}(r,\theta,z,t) = \mathrm{Re}[\{\mathrm{i}\widetilde{u}, \widetilde{v}, \widetilde{w}, \widetilde{p}\}(r)\exp(\mathrm{i}m\theta + \mathrm{i}kz - \mathrm{i}(\sigma_r + \mathrm{i}\sigma_i)t)], \qquad (4.1)$$

where exponential-in-time behaviour is assumed (cf. (2.1), where exponential dependence on time is not assumed). For the Oseen vortex, all eigenmodes are stable, i.e. $\sigma_i = 0$ (figure 7*a*). The eigenmode structure in r is a radially damped

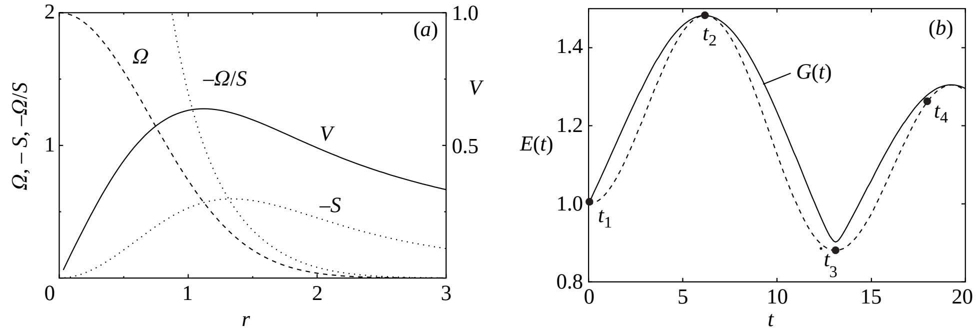

FIGURE 8. (*a*) Profiles of mean velocity V, vorticity Ω, strain rate S and vorticity-to-strain ratio Ω/S (which monotonically increases to infinity at the axis) for an Oseen vortex. (*b*) $G(t)$ and $E(t)$ of the optimal mode for $M=2$, $m=1$, $k=2$ and $Re=10^4$. The perturbations at times t_1–t_4 are shown in figure 10.

oscillation, and the modes can be ranked according to the number of nodes in the radial oscillation (see figure 7*b*, where the first three modes are shown).

It is interesting to see how growing perturbations can be formed via eigenmode superposition. We project an arbitrary perturbation on a basis consisting of a finite number M of the lowest-order eigenmodes. Inserting such a perturbation form in (2.2) results in a discrete matrix representation of the governing linear operator. Initial perturbations maximizing energy growth are then obtained by computing the operator norm via singular value decomposition (see Schmid & Henningson 2001, for details of this technique).

Eigenmodes $m=0$. Consistent with the three-dimensional growth mechanism discussed in § 3, axisymmetric perturbations accumulating large ω_r in the straining region of the mean flow ($r \gtrsim 1$) experience the largest growths. Figure 7(*c*) shows the variation of optimal mode ω_r-profiles as the number M of eigenmodes superposed is increased. Note that each eigenmode individually has its largest amplitude closest to the vortex axis (figure 7*b*); thus, in a superposition, the eigenmodes tend to cancel each other in the vortex core, while constructively interfering outside the core ($r \gtrsim 1$). With increasing M, there is greater cancellation of vorticity within the core and a larger fraction of the enstrophy is located outside the core. Note that volume-integrated radial enstrophy ($\sim r\omega_r^2$) increases with M as ω_r peaks shift to higher r.

To understand this behaviour it is useful to recall the mean flow field of the Oseen vortex (figure 8*a*). The flow comprises a vortical core surrounded by a region of swirling potential flow. Mean vorticity Ω peaks on the axis and the mean strain $S=r(V/r)'$ (which numerically is a negative quantity) at $r \approx 1.2$. The mean azimuthal velocity is maximum at $r \approx 1.1$, which can be considered as the vortex core radius. The vorticity-to-strain ratio increases monotonically with decreasing r.

The location of peak ω_r in figure 7(*c*) thus progressively shifts to regions of weaker vorticity-to-strain ratio. The progressive weakening effect of vorticity allows transient perturbations of increasing M to grow for longer periods of time; figure 7(*d*) shows that the gain $G(t)$ of optimal modes increases with increasing M. Clearly, with increasing M, more 'efficient' interference occurs between the modes.

Eigenmodes $m=1$. Transient growth resulting from the superposition of non-orthogonal eigenmodes is generic to all m. An illustration of the growth of bending waves resulting from an optimal superposition of the first two $m=1$ modes is shown in figure 8(*b*). The amplification is very modest ($G_{max} \approx 1.5$), but expectedly so since

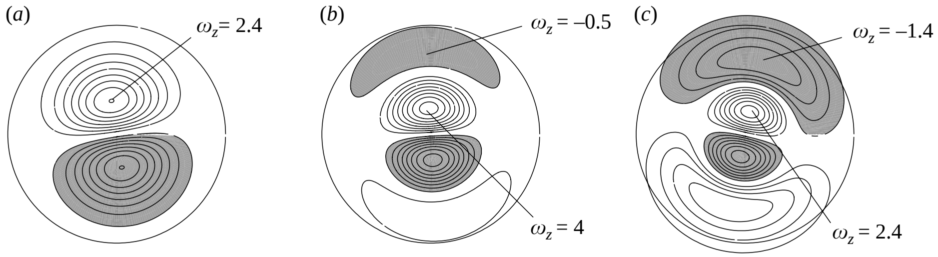

FIGURE 9. ω_z contours of the first two $m = 1$ eigenmodes (*a,b*) of an Oseen vortex and their optimal superposition (*c*), whose energy evolution is shown in figure 8(*b*). Negative ω_z denoted by shading.

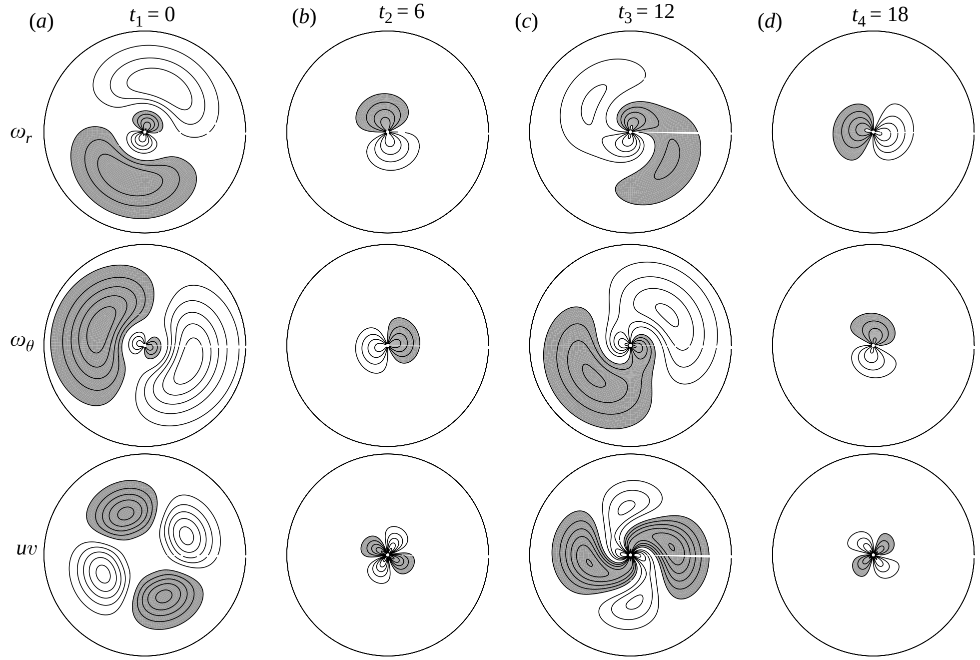

FIGURE 10. Evolution of ω_r, ω_θ and uv contours for the initial condition shown in figure 9(*c*), at times indicated in figure 8(*b*). Shading denotes negative values.

only two decaying modes are superposed. The two eigenmodes and the optimal superposition that grows are plotted in figure 9. The superposition is such that individual eigenmode vorticity fields are additive at large r, whereas they tend to cancel each other at small r. The evolution of the initial condition (figure 9*c*) is plotted in terms of ω_r, ω_θ and uv contours in figure 10 at four stages. These times correspond approximately to the first two maxima and two minima (marked t_1–t_4) of the energy evolution plotted in figure 8(*b*). Initially, there is large ω_r and ω_θ near the core periphery. The flow induced by the ω_θ distribution generates a four-celled pattern of uv contours, as shown in figure 10. There is a nearly symmetric distribution of positive and negative uv, but with slightly larger positive uv magnitudes, hence positive volume-integrated uv. Further, ω_r is tilted toward ω_θ and stretched by the mean strain field (see figure 3*a*). The net effect is energy amplification. The two eigenmodes oscillate at different frequencies, and therefore the phase relationship

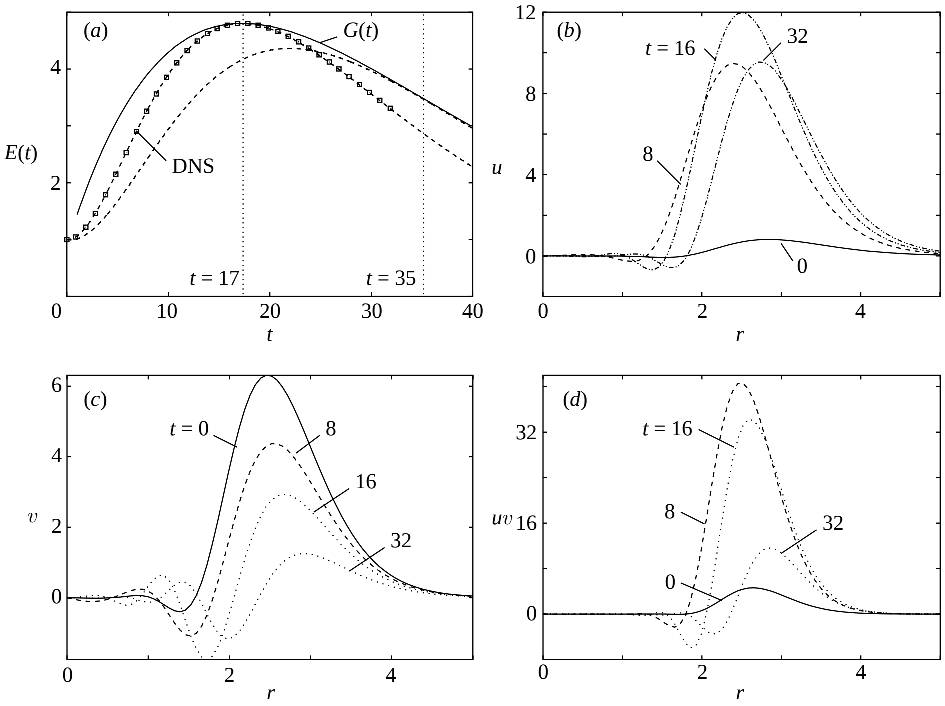

FIGURE 11. (*a*) The gain $G(t)$ and energy evolutions $E(t)$ of $t=17$ global optimal and $t=35$ optimal (dashed curves) of an Oseen vortex. Symbols show $E(t)$ obtained via DNS of the linearized Navier–Stokes equation. Profiles of the global optimal at times $t=0, 8, 16, 32$: (*b*) $u(r)$, (*c*) $v(r)$, and (*d*) $uv(r)$. In all cases, $m=0$, $k=\pi$, and $Re=2000$.

obtaining at $t=0$ is not maintained at later times. At $t\approx 6$, the two eigenmodes cancel each other's vorticity at large r, but are additive at small r (figure 10*b*). Consequently, large vorticity and large uv magnitudes now exist only in the region of near-zero strain (near the axis), and energy production is reduced nearly to zero. At still later times ($t\approx 12$), the original phase relationship is nearly restored, and energy is amplified once again (figure 10*c*). This cyclical growth and decay of energy continues with slow viscous damping.

4.2. *Axisymmetric modes* ($m=0$)

We now consider the growths obtained by solving the transient growth problem (§ 2) and first focus on axisymmetric ($m=0$) optimal modes. Figure 11(*a*) plots a typical gain function, and the energy evolutions of the $t=17$ and $t=35$ optimals, the former being also the global optimal. It also shows the global optimal's energy evolution as computed via DNS – obtained by solving the linearized equations with frozen base flow. Agreement between the two independent calculations is good confirmation of the accuracy of the transient growth numerics. The u and v evolutions for the global optimal perturbation are shown in figure 11(*b*,*c*), and the corresponding ω_r and ω_θ contours are shown in figure 12. The profiles are plotted in the z-plane between two azimuthal vortex filaments (plane z_A in figure 12*a*), where the peaks of u and v are the largest.

In the following, we show that optimal perturbation evolution is in good qualitative agreement with the inviscid mechanisms of growth and its arrest discussed earlier

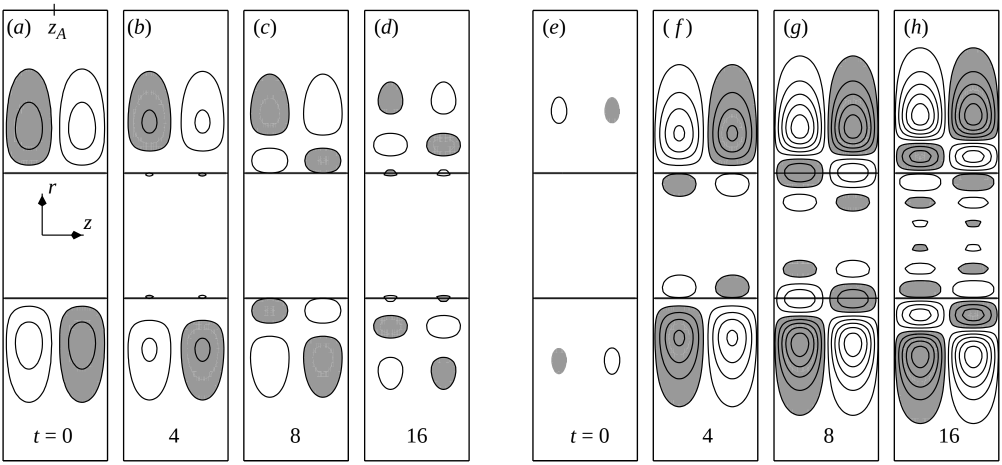

FIGURE 12. ω_r (*a–d*) and ω_θ (*e–h*) contours for an Oseen vortex $m = 0$ optimal mode, figure 11(*b–d*), at times $t = 0, 4, 8, 16$. In all cases, $Re = 2000$, $k = \pi$; contours are plotted with $\omega_{min} = 0.05$ and $\delta\omega = 0.1$. Thick lines denote $\Omega_z = 0.5$ (corresponding to $r \approx 1.3$ in figure 8*a*).

(§ 3.2.3). The initial perturbation energy (enstrophy) of the optimal mode is mainly in the v (ω_r) component, with u (ω_θ) being significantly weaker (figure 11*c* and figure 12*a*). The perturbation is radially localized at the vortex core periphery ($r \approx 1$), i.e. near the region of the largest strain rate $S = r(V/r)'$ (see figure 8*a*). The mean strain tilts ω_r towards ω_θ and stretches the azimuthal vorticity (as illustrated in figure 3*a*), which leads immediately to the growth of radial velocity u (figure 11*b*, at $t = 8$). The growing radial velocity u is localized in the region of large v, as in the case of the model flow in figure 5(*b*). The presence of both positive u and positive v (figure 11*b,c*, at $t = 8$) implies positive Reynolds stress uv (figure 11*d*), hence energy growth. Growth of radial velocity feeds back to cause a decrease in the magnitude of v (compare v profiles at $t = 0$, 8 and 16 in figure 11*c*). The decay of v is the consequence of the progressive depletion of ω_r (figure 12*a–d*) through core dynamics (figure 4*b,c*). (Recall that this nearly 90° phase shift between the growths of $u(r)$ and $v(r)$ is associated with the coiling and uncoiling of vorticity caused by core dynamics (figure 4).) The perturbation Reynolds stress uv now begins to decay (figure 11*d*, at $t = 16$ and 32) – due to, at first, the decay of v (see $t = 16$ profile) and, later, of u as well ($t = 32$ profile). As the Reynolds stress decays, so does the energy growth rate. At $t \approx 17$, the growth of energy is arrested; thereafter the perturbation energy decays through viscous damping.

The perturbation vorticity distribution within the core becomes increasingly oscillatory in r at large times (note the core ω_θ distribution in figure 12*h*). This behaviour can be understood by noting that the initial perturbation contains a large number of eigenmodes, superposed such that the oscillations are cancelled in the vortex core (figure 12*a,e*). Since the eigenmodes are dispersive, their initial phase relationship is not maintained at later times, when the radially oscillatory structure of individual eigenmodes is manifested; see also the associated oscillations in figure 11(*b–d*).

Effects of vorticity and viscosity. For the model flow (3.4) (§ 3.2.4) we have seen that strain-driven amplification is arrested inviscidly by mean vorticity. In the Oseen vortex, there are two additional effects. First, viscous damping also limits transient growth. Second, perturbations localized at different radii experience different periods

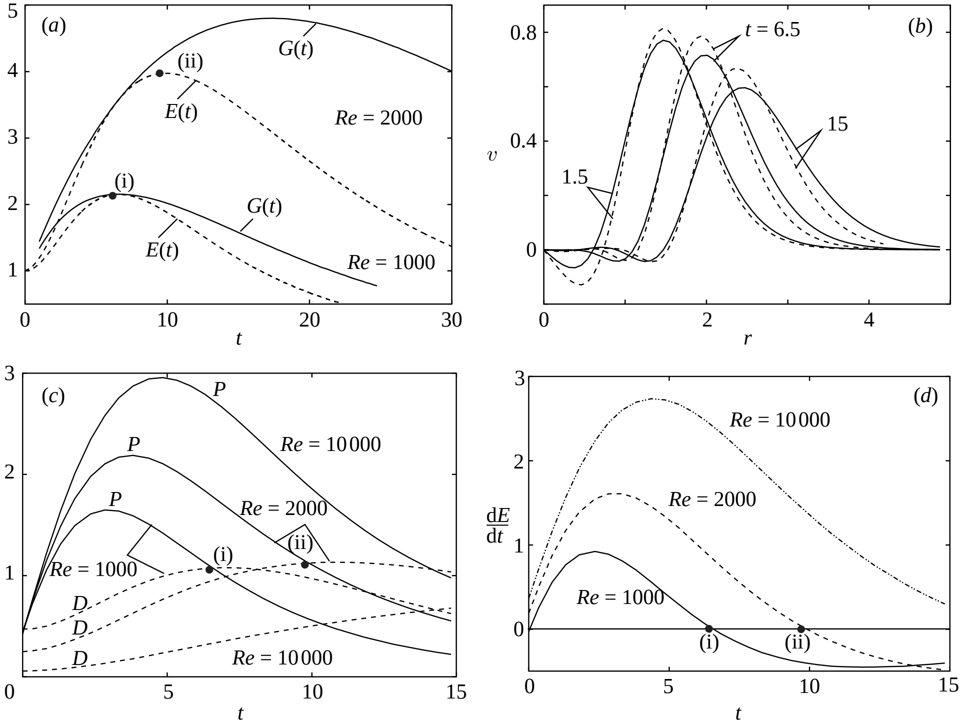

FIGURE 13. (*a*) Gains $G(t)$ and energy evolutions of $t = 6.5$ optimals of an Oseen vortex at $Re = 1000$ and 2000. (*b*) Initial v profiles of various optimals at $Re = 1000$ (solid) and $Re = 2000$ (dashed). (*c*) Volume-integrated production $P(t)$ and dissipation $D(t)$ of perturbation energy, for $t = 6.5$ optimals at $Re = 1000$, 2000, and 10,000. (*d*) Energy growth rate $\mathrm{d}E/\mathrm{d}t$ for the modes in (*c*). In all cases, $m = 0$ and $k = \pi$. Peak energy times for Re = 1000 and 2000 are indicated by (i) and (ii).

of growth because of the radially varying vorticity-to-strain ratio. The competing effects of strain, vorticity, and viscous damping select a preferred radius of optimal perturbation localization. This competition also explains the characteristic shape of the gain curve $G(t)$ (e.g. figure 11*a*), which first increases with the growth period (for $t < t_{max}$) and later drops ($t > t_{max}$).

Figure 13(*b*) shows the initial v profiles for three optimals: $t = 1.5$, $t = 6.5$ and $t = 15$, at two vortex Reynolds numbers Re ($\equiv$ circulation/viscosity) of 1000 and 2000. The $t = 6.5$ mode is the global optimal at $Re = 1000$. Being optimal at small t, a perturbation grows rapidly. Rapid growth implies that the perturbation is located close to the core periphery, where the strain rate is the largest. Such localization indeed occurs for the $t = 1.5$ optimal. Now, in addition to the strain rate, the vorticity-to-strain ratio also increases with decreasing r (figure 8*a*). This means that the vorticity-induced arrest of growth occurs faster for modes localized near the core. Consequently, perturbations that are optimal at progressively larger times originate at progressively larger distances from the vortex axis (this trend is clear from the $t = 1.5$, $t = 6.5$ and $t = 15$ optimal mode profiles in figure 13*b*).

Energy amplification being proportional to the growth rate as well as to the period of growth, the preceding arguments do not explain why the $t = 6.5$ mode amplifies more than the $t = 1.5$ mode. It turns out that, since mean vorticity decays exponentially ($\Omega \sim \exp(-r^2)$) and the strain rate only algebraically ($S \sim r^{-2}$), the inviscid arrest of growth by vorticity can be progressively weakened (relative to amplification by strain) in modes that originate at progressively larger radii. (Quantitative analysis of this effect is presented in § 4.2.1.) Hence the larger growth of the $t = 6.5$ optimal.

But why is growth reduced for the $t = 15$ optimal? The reduction is caused by viscous damping. To see this, we compare the gains $G(t)$ at $Re = 1000$ and 2000 (figure 13*a*). At $Re = 2000$, $G(t = 15) > G(t = 6.5)$, whereas the opposite is true at $Re = 1000$. As shown in the following, with increasing Re, the weakening viscous damping allows faster and longer growth of transient perturbations. Thus, while both $t = 6.5$ and $t = 15$ optimals experience increasing gain with increasing Re, the weaker vorticity-induced damping for the $t = 15$ optimal allows it to amplify more than the $t = 6.5$ optimal.

Viscous effects can be studied by plotting the time-evolutions of volume-integrated energy production P and dissipation D (figure 13*c*), which appear in the perturbation energy equation:

$$\mathrm{d}E/\mathrm{d}t = P - D.$$

Here

$$P = -\int uv\, r(V/r)'\, \mathrm{d}V, \qquad D = 2\nu \int s_{ij}s_{ij}\, \mathrm{d}V,$$

with

$$\begin{aligned} s_{ij}s_{ij} = \; & (\partial u/\partial r)^2 + (\partial u/r\partial\theta - v/r)^2 + (\partial u/\partial z)^2 \\ & + (\partial v/\partial r)^2 + (\partial v/r\partial\theta + u/r)^2 + (\partial v/\partial z)^2 \\ & + (\partial w/\partial r)^2 + (\partial w/r\partial\theta)^2 + (\partial w/\partial z)^2 . \end{aligned}$$

Initial growth rates are close at $Re = 1000$ and 2000 (figure 13*d*), as expected, since the perturbations are nearly identical (figure 13*b*). Viscous cross-diffusion of vorticity in adjacent counter-rotating azimuthal vortex filaments outside the vortex column core diminishes ω_r and ω_θ magnitudes. The reduced ω_r further reduces ω_θ amplification; see equation (3.9). Since ω_θ-induced radial motion produces $uv > 0$ (figure 3*b*), the Reynolds stress magnitude is smaller at lower Re, where viscous cross-diffusion is higher. Thus P, and hence energy growth rate, is arrested more rapidly at lower Re (figure 13*c*,*d*). Simultaneously, viscous dissipation of perturbation energy, at early times, is also larger at lower Re (because initially the perturbations are nearly identical, and so also are their s_{ij}). The net effect is that the time of intersection of the dissipation and production curves – which signals the end of energy growth – increases with increasing Re (see points i, ii in figure 13). This trend of faster ($P - D$ is larger) and longer (the P, D crossing-point is at greater times) transient growth persists with further increase of Re: see the $Re = 10^4$ curves in figure 13(*c*,*d*).

In summary, the radial inhomogeneity of the vorticity-to-strain ratio causes optimal perturbations to be localized at a preferred radius, which increases with increasing period of growth. Perturbations close to the axis experience rapid growths for short durations of time; vice versa for perturbations originating far from the axis. Starting from small growth periods t, the increase in $G(t)$ with t is due to the weakening arrest by mean vorticity. The gains increase until a critical radius is reached, where $G(t)$ is maximized. For larger t, viscous damping is then responsible for the decrease of $G(t)$.

Optimal gain. We now turn to the variation of G_{max} with m, k and Re. G_{max} is obtained by searching for the first local maximum of $G(t)$ for each specific set of values of the parameters: m, k and Re. While it is not guaranteed that this search produces the global maximum, examination of several individual $G(t)$ curves indeed

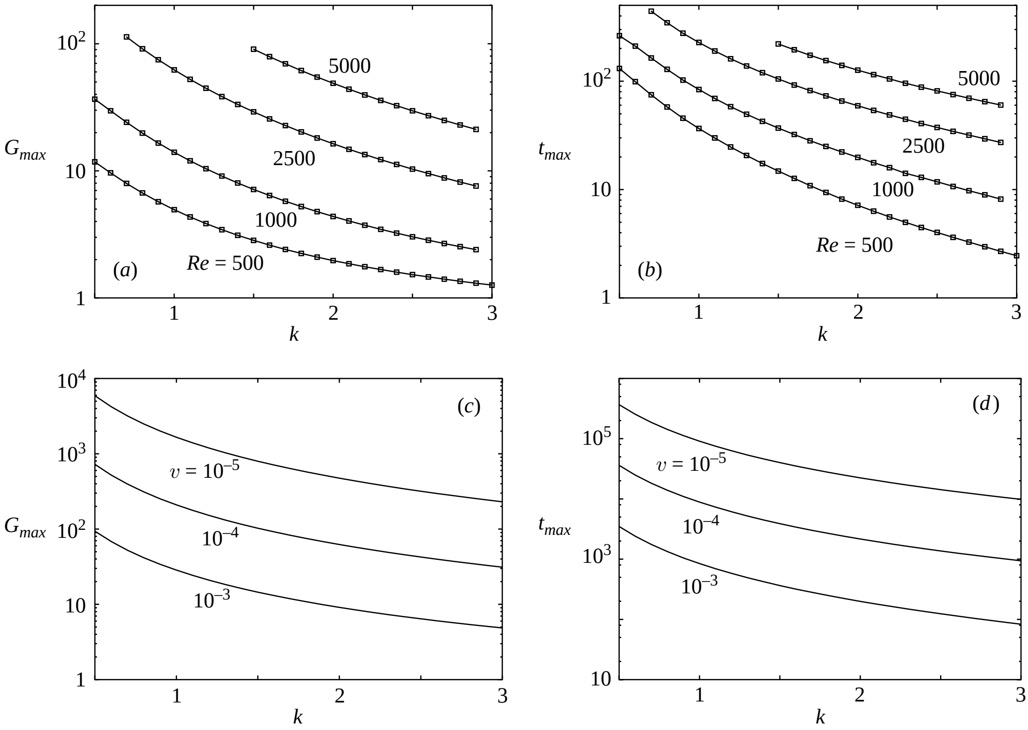

FIGURE 14. Optimal gains G_{max} (a) and times t_{max} (b) for Oseen vortex $m = 0$ modes, as functions of k and Re. Results from modelling analysis of G_{max} (c) and t_{max} (d).

showed the first local maximum also to be the global maximum (see, for instance, the $M = 10$ curve in figure 7b). Figure 14(a,b) plots the variation of G_{max} and t_{max} with axial wavenumber k for $m = 0$ modes. A 100-fold increase of energy occurs even at the very moderate $Re = 2500$ – remarkable in a normal-mode-stable flow. Note that practical flows feature vortices at much higher Re; aircraft wake vortex Re is about four orders of magnitude higher. All our computations show increasing G_{max} with increasing Re, as seen in figure 14(a), strongly suggesting that *transient growth plays an important role in the evolution of flows dominated by intense vortices.*

With decreasing k, there is a sharp increase in the maximum amplification achieved (note logarithmic ordinate), and this trend seems to extend to the limit $k \rightarrow 0$. Such behaviour is noteworthy because no transient growth is possible for a two-dimensional ($k = 0$) axisymmetric mode, and thus the $k \rightarrow 0$ limit would appear to be singular. As will be seen in the following, the growth rate in the $k \rightarrow 0$ limit does approach zero, but since the growth period of these modes approaches infinity (see figure 14b), the energy gain can be finite, and indeed large. These slowly growing modes are localized far away from the vortex axis. In an isolated vortex, the perturbation can originate at arbitrarily large radial distances from the core. Both the viscous and inviscid growth-arresting effects, discussed earlier, can thereby be weakened increasingly with increasing perturbation radius, allowing very large energy growths. Confirmation of such limiting behaviour is numerically infeasible and would require asymptotic analysis. While more rigorous analysis is warranted, a simplified model of the competing effects of strain (in amplifying perturbation energy) and of viscosity and vorticity (in dampening the growth) is presented below. The model captures fairly well the variations of G_{max} with ν and k, including the $k \rightarrow 0$ limit.

4.2.1. *Analysis of* $G_{max}(\nu, k)$ *trends*

Let us consider the coupled system of equations (3.3) governing the evolutions of u and v. Note that the right-hand-side term in the u equation, $2V/r = \mathscr{D}V - r(V/r)'$, equals $\Omega - S$, where Ω is the mean vorticity and S is the mean strain rate. We simplify the equations by neglecting the spatial derivative operator in the u-equation. This approximation is justified because the radial variation of u is similar to that of v at early times, when v is sharply localized (see figure 11*b,c*). Including viscous effects gives the following simplified model of u and v dynamics:

$$\frac{\mathrm{d}}{\mathrm{d}t}u = (\epsilon + s)v - \nu k^2 u, \quad \frac{\mathrm{d}}{\mathrm{d}t}v = -\epsilon u - \nu k^2 v. \tag{4.2}$$

Here, ϵ is the modelled mean vorticity, s the modelled mean strain rate (taken to be a positive quantity), and ν the viscosity. Note that the viscous term has been simplified by assuming that all the spatial derivative terms are of the same order. These model equations retain two key properties of the exact equations: first, u is driven by v when there is either non-zero mean vorticity or non-zero mean strain rate, and, second, v is coupled to u only in the case of non-zero vorticity. That is, the mean strain causes a perturbation with initial v (associated with ω_r) to experience growth of ω_θ (hence u) through vortex stretching (§ 3.2.1), whereas mean vorticity mutually couples u and v: that is, while v drives u, as in the case of pure straining flow, here u also drives the evolution of v. This leads to oscillatory perturbation evolution (i.e. core dynamics, § 3.2.2).

Assuming that initially the radial velocity u is zero and $v(t=0) = v_0$, (4.2) has the solution

$$u = v_0 \sqrt{1 + \frac{s}{\epsilon}} \exp(-\nu k^2 t) \sin \gamma t, \quad v = v_0 \exp(-\nu k^2 t) \cos \gamma t, \tag{4.3}$$

where $\gamma = \epsilon\sqrt{1 + s/\epsilon}$. The solution shows that the radial and azimuthal velocity components are damped by viscosity, oscillating out of phase with each other, with frequency γ.

Let us first consider the inviscid case. The radial velocity component attains a peak amplitude of $v_0\sqrt{1 + s/\epsilon}$, where s/ϵ can be interpreted as the strain-to-vorticity ratio at the radial location of the initial perturbation. Now, in an Oseen vortex, the mean vorticity decays exponentially at large r, i.e. $\Omega \sim \exp(-r^2)$, whereas the strain rate decays only algebraically, i.e. $S \sim 1/r^2$; the strain-to-vorticity ratio can therefore be made arbitrarily large by locating the perturbation sufficiently far away from the vortex axis. In this limit, $\gamma \rightarrow 0$ as both ϵ and s become small; that is, the perturbation experiences a long period of growth. Since u becomes much larger than v_0, most of the total perturbation energy is due to the radial velocity component. The maximum gain can thus be estimated to be $G \sim s/\epsilon$, this value being attained as $t \rightarrow \infty$. That is, *optimal perturbations for an inviscid vortex – originating infinitely far away from the vortex axis – experience unbounded amplification with an infinitesimal growth rate.*

In viscous flows, on the other hand, viscosity limits growth because perturbations will be damped when the inviscid rate of amplification becomes much smaller than the viscous rate of damping, $s \ll \nu k^2$. Thus viscosity sets the largest radius of localization of a growing perturbation, i.e. sets r such that $s \sim \nu k^2$. Viscous damping also means that the gain can no longer be infinite. To calculate the optimal gain, we note that

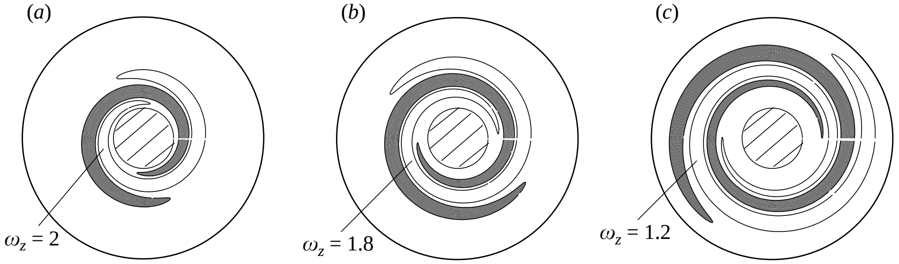

FIGURE 15. ω_z contours for (*a*) $t = 20$ ($G = 15$), (*b*) $t = 62$ ($G = 35$), and (*c*) $t = 120$ ($G = 20$) Oseen vortex optimals with $m = 1$, $k = 2$ and $Re = 5000$. Shaded regions denote negative ω_z and hatched circular contour is $\Omega = 1$.

radial velocity in (4.3) is maximized at time

$$t_g = \frac{1}{\gamma} \tan^{-1} \frac{\gamma}{\nu k^2},$$

with the maximal gain being

$$G \sim \left(1 + \frac{s}{\epsilon}\right) \exp(-2\nu k^2 t_g) \sin^2 \gamma t_g.$$

By maximizing this gain expression over the radial location of the perturbation (hence over s or ϵ) – for given values of ν and k – one can extract the modelled behaviour of G_{max} (the globally optimal gain, obtained by searching for the largest value of G) and t_{max}. These numerical solutions are plotted in figure 14(*c,d*). Comparison with the actual optimal mode G_{max} and t_{max} curves in figure 14(*a,b*) shows that the model (4.2) captures the trend and hence the physical mechanisms at play, at least qualitatively.

In summary, this simple analysis shows that: (*a*) there can be infinite gain in the inviscid limit, although taking infinite time as the growth rate goes to zero; and (*b*) viscosity, together with vorticity, acts both to limit the gain and to set the radial location of the optimal perturbations. Among all optimals, the largest-growth modes are not necessarily the most significant, because (*a*) the growth rates become very small, and the modes can be overwhelmed by faster growing perturbations; and (*b*) the modes are located very far from the vortex axis and hence may not be relevant in typical flows where individual vortices do not exist in isolation. It should also be noted that with increasing radius of perturbation localization, results from linear analysis remain applicable only to perturbations with progressively diminishing amplitudes. This is because $V \to 0$ as $r \to \infty$ and linear analysis assumes $u, v, w \ll V$. Thus, the global optimals discussed in the preceding would have to be of such small initial amplitude that their growth is unlikely to trigger significant nonlinear effects.

4.3. *Helical bending wave modes* ($m = 1$)

Having examined optimal mode growth mechanisms in the axisymmetric case, we now turn to the bending wave ($|m| = 1$) modes. The perturbation vorticity is radially localized, and, as in the $m = 0$ case, the combined effects of amplification by strain, competing with damping by vorticity and viscosity, determine the time-period and magnitude of gain. To illustrate this, let us consider optimal modes with different growth periods. Figure 15 plots axial vorticity perturbation ω_z for three optimal modes, with $t = 20$, 62 and 120, all for the same values of k and Re. The intermediate mode is the global optimal. The structure of ω_z in all three is in the form of spiral patterns of contours with positive tilt. The associated streamlines contribute positive

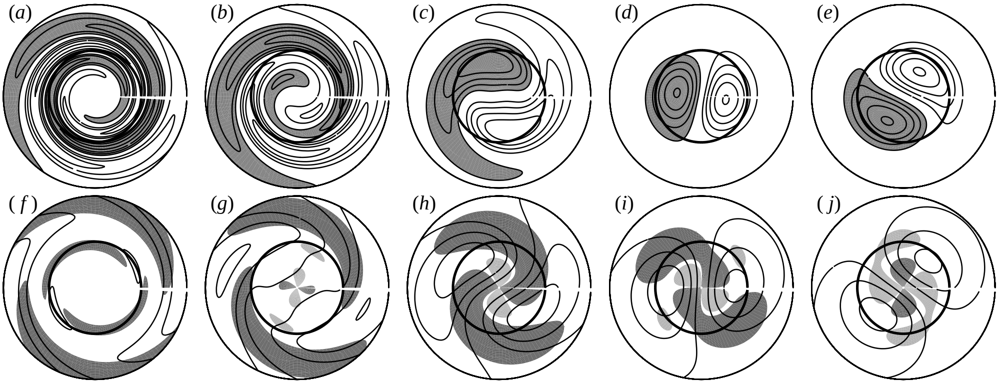

FIGURE 16. Long-wavelength $k = 0.1$, $m = 1$ bending wave mode at $Re = 5000$. ω_z contours (*a–e*) and streamlines projected on the (r,θ)-plane (*f–j*) for Oseen vortex $t = 15$ optimal. Shaded regions in (*a–h*) denote $\omega_z < 0$; in (*f–j*) light-shaded regions denote $uv < 0$ and dark-shaded regions $uv > 0$. Times plotted are 0, 5, 10, 15, 20 in each row. Thick inner circle in each panel is mean vorticity $\Omega = 1$.

uv, accounting for perturbation energy growth. The $t = 20$ mode, being localized in the region of largest strain, experiences the fastest growth, but the growth is soon arrested by the large vorticity-to-strain ratio at this location. On the other hand, the $t = 120$ mode grows slowly but for a longer period of time. Its growth is arrested eventually by viscous damping. The similarity of ω_z distributions indicates that the physical growth mechanisms in all three cases are similar and independent of t.

We shall demonstrate in the following that a combination of ω_z shearing (§ 3.1) (absent for $m = 0$) and ω_r, ω_θ vortex stretching/tilting mechanisms account for the growth and decay of transient $m = 1$ perturbations.

Long-wavelength mode. The shearing mechanism, being inherently two-dimensional, may be expected to dominate the tilting/stretching mechanism when k is small. To isolate this mechanism, we therefore consider a long-wavelength bending wave. Figure 16 plots the evolution of ω_z (panels *a–e*) and perturbation streamlines (panels *f–j*) projected on the (r,θ)-plane, for a $k = 0.1$ optimal perturbation. Initially, $\omega_z \gg \omega_r, \omega_\theta$, as expected due to the quasi-two-dimensionality of this mode. Initial ω_z contours are positive-tilt spirals (figure 16*a*) that induce a flow having positive-tilt streamlines (figure 16*f*). The net positive uv in this perturbation leads to energy growth, via the $-uvr(V/r)'$ term in the perturbation energy equation (3.1). Differential azimuthal advection of ω_z by the mean flow diminishes the positive tilt of the ω_z contours and perturbation streamlines, i.e. $\mathrm{d}r/\mathrm{d}\theta$ of these curves is progressively reduced. Such evolution, evident at times $t = 5$ (figure 16*b,g*) and $t = 10$ (figure 16*c,h*), is very similar to that of the model flow discussed in figure 2. Consequently, net positive uv is reduced and regions with significant negative uv emerge (figure 16*h*). Unlike the pure-straining mean flow discussed in § 3, vorticity in the Oseen vortex promotes the development of oscillatory bending waves. The characteristic pattern of perturbation vorticity associated with a bending wave is evident from the closed patterns of ω contours and perturbation streamlines at later times (figures 16*c–e* and 16*h–j*). These closed cells are rotated around the vortex with relatively little change in perturbation structure (figure 16*d,e*). The flow now contains nearly equal positive and negative uv (figure 16*i,j*), and thus energy growth is arrested and the perturbation undergoes slow decay due to viscous damping.

It should be noted that while the shearing mechanism of growth is dominant for this small k, the effects of three-dimensionality are not insignificant. For instance, peak ω_z, which must remain constant in a purely two-dimensional flow, grows three-fold during the evolution shown in figure 16. Growth of ω_z can be qualitatively understood by examining the vorticity equations:

$$\frac{\partial \omega_r}{\partial t} + \frac{V}{r}\frac{\partial \omega_r}{\partial \theta} = \Omega \frac{\partial u}{\partial z}, \tag{4.4}$$

$$\frac{\partial \omega_\theta}{\partial t} + \frac{V}{r}\left(\frac{\partial \omega_\theta}{\partial \theta} + \omega_r\right) = \underbrace{\omega_r \frac{\partial V}{\partial r}}_{\text{`stretching'}} + \Omega \frac{\partial v}{\partial z}, \tag{4.5}$$

$$\frac{\partial \omega_z}{\partial t} + \underbrace{\frac{V}{r}\frac{\partial \omega_z}{\partial \theta}}_{\text{`shearing'}} + u\frac{\mathrm{d}\Omega}{\mathrm{d}r} = \Omega \frac{\partial w}{\partial z}. \tag{4.6}$$

Note that all three vorticity components are coupled through the vortex tilting/stretching terms. In addition to the 'shearing' and tilting/stretching effects (identified in the equations above) isolated in the model flows of § 3, additional advection and tilting terms are present in the full equations. In early stages of the evolution in figure 16, the shearing term is dominant and leads to deformation of the ω_z contours. The stretching term $\Omega \partial w/\partial z$ in the ω_z equation is initially negligible, because of weak axial velocity. With time, the magnitude of ω_r and ω_θ increases because of the tilting of mean vorticity into the (r,θ)-plane (through the terms $\Omega \partial u/\partial z$ and $\Omega \partial v/\partial z$, respectively) by ω_z-induced u and v. In turn, ω_r and ω_θ induce axial velocity w, which strengthens progressively. This leads to the growth of peak ω_z through the $\Omega \partial w/\partial z$ term. (Note that these terms vary sinusoidally in z and θ; depending on m and k, the magnitude of the vortex stretching and tilting terms will depend on θ at each z. But the same arguments apply at each z.)

Short-wavelength mode. In contrast to the long-wavelength mode just discussed, large-k modes grow predominantly through the three-dimensional mechanism of vortex tilting/stretching. We discuss mode evolution in terms of optimal mode vorticity fields (figure 17) and simplified schematics elucidating the essential vortex dynamics (figure 18). In figure 17, panels (*a–e*) plot ω_r, (*f–j*) plot ω_θ, and (*k–o*) plot ω_z. Perturbation energy for this mode is maximum at $t = 60$ (panels *d,i,n*). The initial perturbation vorticity is dominated by ω_r and ω_z, when ω_θ is much weaker (figure 17*a,f,k*). To understand subsequent dynamics, let us consider a fluid particle A (figure 18*a*) which has only ω_r and ω_z. As the particle is advected around the vortex core, vorticity is tilted from the radial towards the azimuthal direction and stretched, because of differential advection, as illustrated in figure 3. This effect is described by the $\omega_r \partial V/\partial r$ term in (4.5). Thus, ω_θ, absent initially, appears outside the vortex core (figure 17*g*). In turn, ω_θ leads to the growth of ω_r and ω_θ within the core (see figure 17*c,h*).

To understand this, let us consider the governing equations for perturbation vorticity at the vortex axis, where the dynamics are simplified because the advection terms vanish. These equations are

$$\frac{\partial \omega_x}{\partial t} = -\frac{\Omega_0}{2}\omega_y + \Omega_0 \frac{\partial u_x}{\partial z}, \quad \frac{\partial \omega_y}{\partial t} = \frac{\Omega_0}{2}\omega_x + \Omega_0 \frac{\partial u_y}{\partial z}, \quad \frac{\partial \omega_z}{\partial t} = 0, \tag{4.7}$$

where Ω_0 is the mean vorticity on the axis. Here, we use Cartesian components (see figure 18*a* for the coordinate system) to avoid the singularity associated with

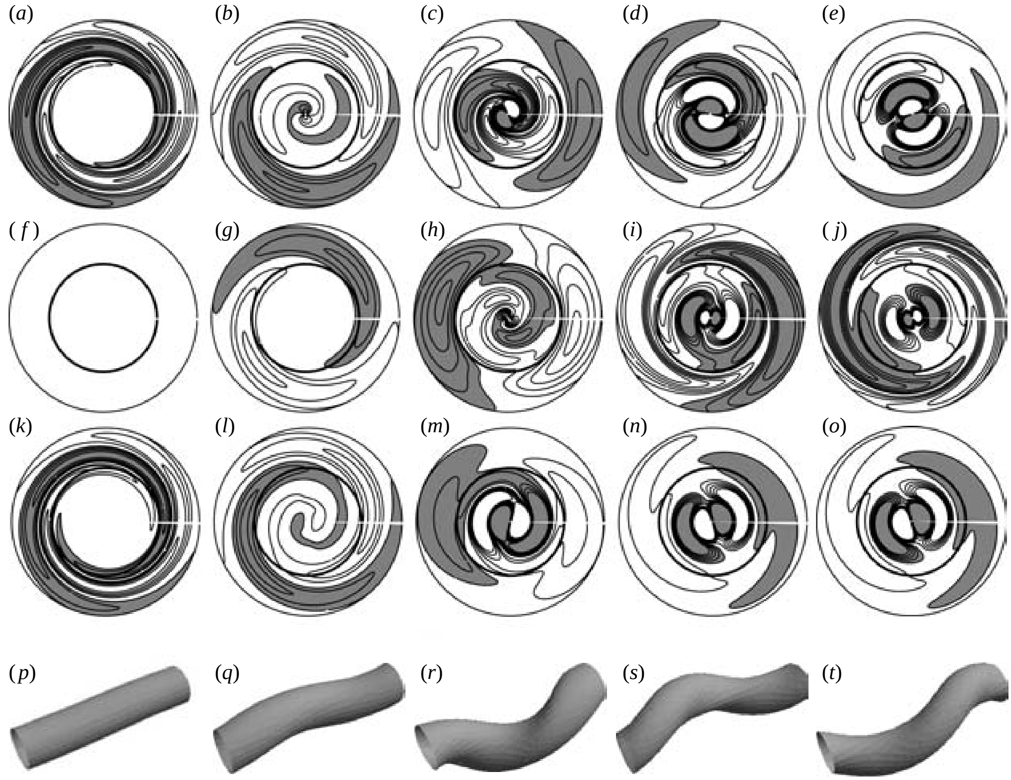

FIGURE 17. Vorticity contours and surfaces for Oseen vortex $m=1$, $t=60$ optimal at times (running left to right) $t=0, 15, 30, 60$ and 90: (*a–e*) contours of ω_r, (*f–j*) ω_θ, (*k–o*) ω_z, and (*p–t*) total vorticity $\Omega + \omega$ surfaces. Shaded regions in (*a–o*) denote negative vorticity and thick contour is $\Omega = 0.2$, indicative of the vortex core. Contour levels are $[\pm 0.2, \pm 1, 0.2]$ for ω_r, $[\pm 1, \pm 5, 1]$ for ω_θ and $[\pm 0.4, \pm 2, 0.4]$ for ω_z, at all times shown. Here $k=2$ and $Re=5000$.

cylindrical coordinates at $r=0$. The first right-hand-side terms in the ω_x and ω_y equations describe the rotation of the perturbation vorticity vector by the mean swirl, whereas the second terms describe the tilting of mean vorticity into the (x,y)-plane by the axial gradient of the perturbation velocity. Note that ω_z must be identically zero on the axis for $m \neq 0$ modes. Now, two fluid particles outside the vortex core (say, A and B in figure 18*b*) separated azimuthally by 180° possess ω_r of opposite sign and also acquire ω_θ of opposite sign, because of the $m=1$ azimuthal variation of the mode. The azimuthal alignment of the vortex filaments at particles A and B induces a flow with non-zero $\partial u_x/\partial z$ on the vortex axis, as illustrated in figure 18(*c*). This perturbation velocity field tilts the mean vorticity $\boldsymbol{\Omega}$ into the x-direction (figure 18*d*), producing ω_x. In turn, this tilted ω_x on the axis induces u_y, whose axial gradient $\partial u_y/\partial z$ causes the tilting of mean vorticity $\boldsymbol{\Omega}$ into the negative y-direction (figure 18*e*), through the $\Omega_0 \partial u_y/\partial z$ term in (4.7), producing negative ω_y. This process of mean vorticity tilting causes generation of in-plane (r,θ-plane) perturbation vorticity $\boldsymbol{\omega}_\perp$ ($\equiv \omega_r \hat{r} + \omega_\theta \hat{\theta}$, which is also $\omega_x \hat{x} + \omega_y \hat{y}$ in the x,y-plane; figure 18*e*), also seen in figure 17(*b–d*,*g–i*). Simultaneous with this generation is the tilting by the mean flow $V(r)$ of $\boldsymbol{\omega}_{\perp 1}$, contributing to $\boldsymbol{\omega}_{\perp 2}$, as illustrated in figure 18(*f*). The tilting of the accumulated $\boldsymbol{\omega}_{\perp 1}$ is evident in terms of the rotation of the ω_r and ω_θ contour patterns in figures 17(*c–e*)

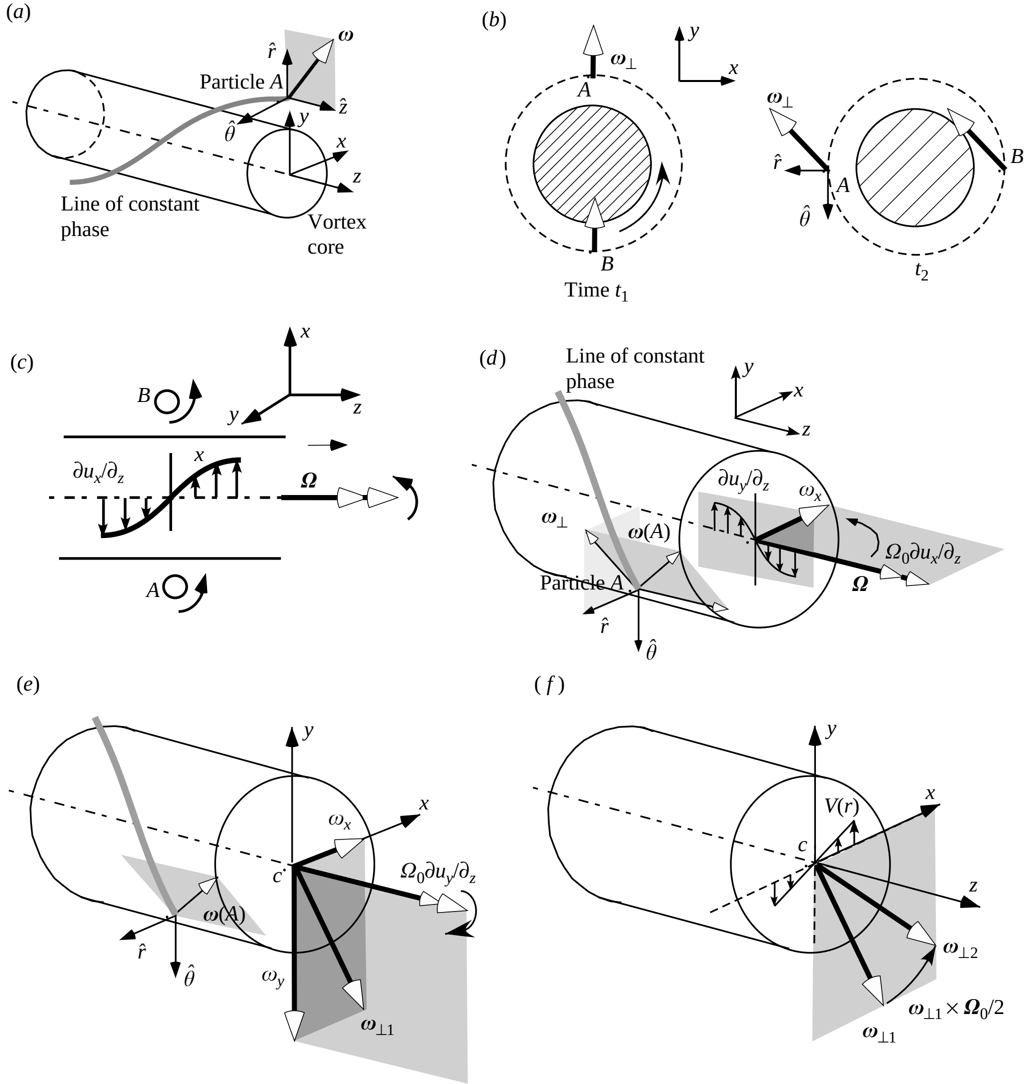

FIGURE 18. Schematic of bending-wave transient growth evolution: (*a*) initial perturbation with vorticity predominantly in the r and z components; (*b*) generation of ω_θ by differential advection; (*c*) flow induced within the core by external helical vortex filaments; (*d*) generation of core vorticity perturbation through tilting of mean vorticity; (*e*) tilting of $\boldsymbol{\omega}_{\perp 1}$ resulting from tilting of $\boldsymbol{\Omega}$ by velocity perturbation, and (*f*) tilting of $\boldsymbol{\omega}_{\perp 1}$ to $\boldsymbol{\omega}_{\perp 2}$ through azimuthal advection by the mean flow (both involving no stretching).

and 17(*h*–*i*). Note that this progressive accumulation of $\boldsymbol{\omega}_\perp$ in the core involves only tilting, but no stretching.

In summary, the dynamics of in-plane vorticity $\boldsymbol{\omega}_\perp$ comprise two effects: first, the accumulation of $\boldsymbol{\omega}_\perp$ through the tilting of $\boldsymbol{\Omega}$; and second, the rotation of accumulated $\boldsymbol{\omega}_\perp$ by the mean swirl. Strong growth of $\boldsymbol{\omega}_\perp$ can occur through resonance (see § 4.3.1).

Role of streamline tilt. While the tilting of ω_r into ω_θ is associated with the generation of $uv > 0$ causing growth of perturbation, additional energy growth occurs through the flow induced by ω_z. This vorticity component induces a positive-tilt-streamline flow in the (r,θ)-plane. With time, the perturbation vorticity field becomes increasingly

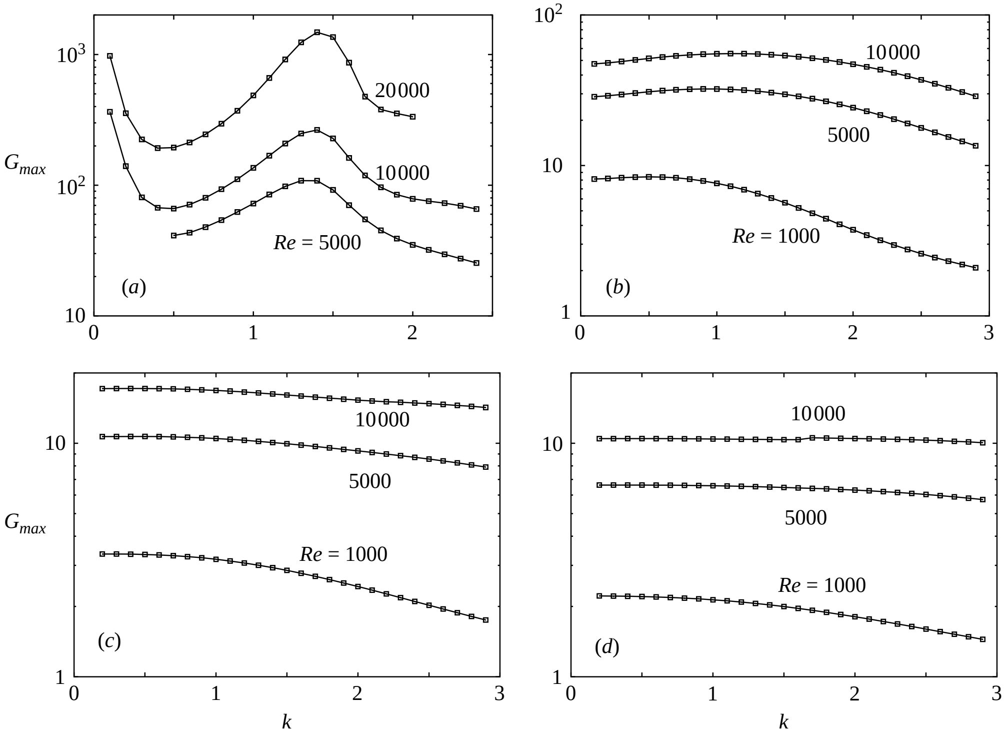

FIGURE 19. Oseen-vortex optimal gains G_{max} for (*a*) $m=1$, (*b*) $m=2$, (*c*) $m=3$, and (*d*) $m=4$.

wave-like, as signalled by the strong growth of vorticity in the vortex core (the region contained within the thick Ω contour) and the rotation of the vorticity contour patterns (see figures 17*d–e*, 17*i–j*, and 17*n–o*). Also, the contours of ω_z are progressively transformed through the shearing mechanism to those inducing streamlines of negative tilt, reducing production. This is the mechanism of cessation of transient growth. Three-dimensional views of the total vorticity field show the generation of a bending wave that deforms the initially rectilinear vortex column (figure 17*p* to figure 17*r*) and subsequent wave rotation (figure 17*r* to figure 17*t*).

Optimal gain. Figure 19(*a*) plots the variation of G_{max} with k for bending waves. There is substantial transient growth, with up to 1000-fold amplification at $Re=20\,000$. Amplifications increase with increasing Re because the growth mechanism is inviscid. These G_{max} curves agree well with those of Antkowiak & Brancher (2004). For given k and Re, G_{max} is smaller for bending waves than for $m=0$ (figure 14*a*). This is due to the increased viscous damping at larger $|m|$; see (2.3*b*). Consistent with this, growth at fixed k and Re decreases with increasing m, as seen from figure 19(*b,c,d*); e.g. while bending wave amplification is more than a 100-fold at $k=1.5$ and $Re=10^4$, the $m=4$ modes experience only a 10-fold amplification.

The bending wave is noteworthy for the sharp peak in G_{max} at an intermediate axial wavenumber ($k\approx 1.3$), in addition to the peak as $k\rightarrow 0$. Antkowiak & Brancher speculate that such a peak could result from a resonance phenomenon, analogous to the resonance-driven transient growth found in plane shear flows (Gustavsson & Hultgren 1980), occurring when the oscillation frequency of an Orr–Sommerfeld eigenmode matches that of a 'Squire' mode (see e.g. Schmid & Henningson 2001).

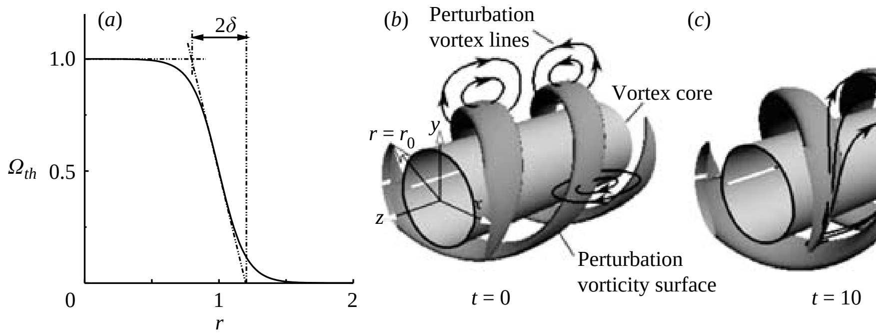

FIGURE 20. (*a*) Mean vorticity Ω_{th} profile for the top-hat vortex (4.8). Perturbation vorticity isosurfaces ('ribbons') and computed vortex lines at $t = 0$ (*b*) and $t = 10$ (*c*). Although $\delta = 0.1$ is used for all calculations, including (*b*) and (*c*), it is 0.2 in the illustrative diagram (*a*).

In the case of the Oseen vortex, the external vortex filaments induce velocity and pressure perturbations within the core that excite the vortex's eigenmodes. Resonance can occur if the external forcing oscillates with the same frequency as that associated with a given core wave. Then, $\boldsymbol{\omega}_{\perp}$ generated by the core wave will be continually reinforced by the $\boldsymbol{\omega}_{\perp}$ induced by the external filament. This leads to sustained growth of core vorticity perturbation (discussed in § 4.3.1).

Since, apart from the tilting of ω_r into ω_θ, the external filaments evolve primarily through advection by the mean flow, oscillation frequency matching would require that the wave oscillation frequency be in the range of the vortex's angular velocities. This is indeed the case for $|m| = 1$ eigenmodes, and makes the resonance scenario a distinct possibility.

4.3.1. *Resonance-driven growth*

To explore resonance-driven transient growth in a vortex, we consider a simplified Rankine-like vortex model, in which the perturbation vorticity dynamics outside the core comprise only two effects: the tilting of ω_r into ω_θ, and the advection of $\boldsymbol{\omega}$ by the mean flow. The tilting of mean flow vorticity by perturbation velocity is absent because $\boldsymbol{\Omega}$ is identically zero outside the core. We consider a top-hat vortex with tan-hyperbolic mean vorticity profile (figure 20*a*):

$$\Omega_z = \tfrac{1}{2}\left[1 - \tanh\left((r - r_{th})/\delta\right)\right], \tag{4.8}$$

where r_{th} is core radius and 2δ is the radial thickness over which the mean vorticity changes from 1 to 0. In the following, $r_{th} = 1$ and $\delta = 0.1$.

Considering perturbations of the form (4.1), the eigenvalue spectrum for this vortex is computed using a matrix method with Chebyshev discretization. The dispersion curves (the real part of the growth rate σ_r as a function of the axial wavenumber k) for the first few lowest-order $m = 1$ eigenmodes are plotted in figure 21(*a*). These curves for the top-hat vortex are, as expected, nearly identical to that of a Rankine vortex (see Saffman 1992). The eigenmodes can be classified into two groups. When observed in a frame rotating with the core-fluid angular velocity, 'co-grade' modes (branches C_1–C_3 in figure 21*a*) are those that rotate in the same direction as the mean flow; 'retro-grade' modes (branches R_0–R_3) rotate in the opposite direction. For $i > 0$, R_i and C_i are conjugate branches, i.e. the eigenvalues on these branches are related through a complex conjugacy, whereas R_0 is a degenerate branch, having no co-grade conjugate. Note that $-0.5 \leqslant \sigma_i \leqslant 1.5$, whereas the vortex angular velocity equals 0.5

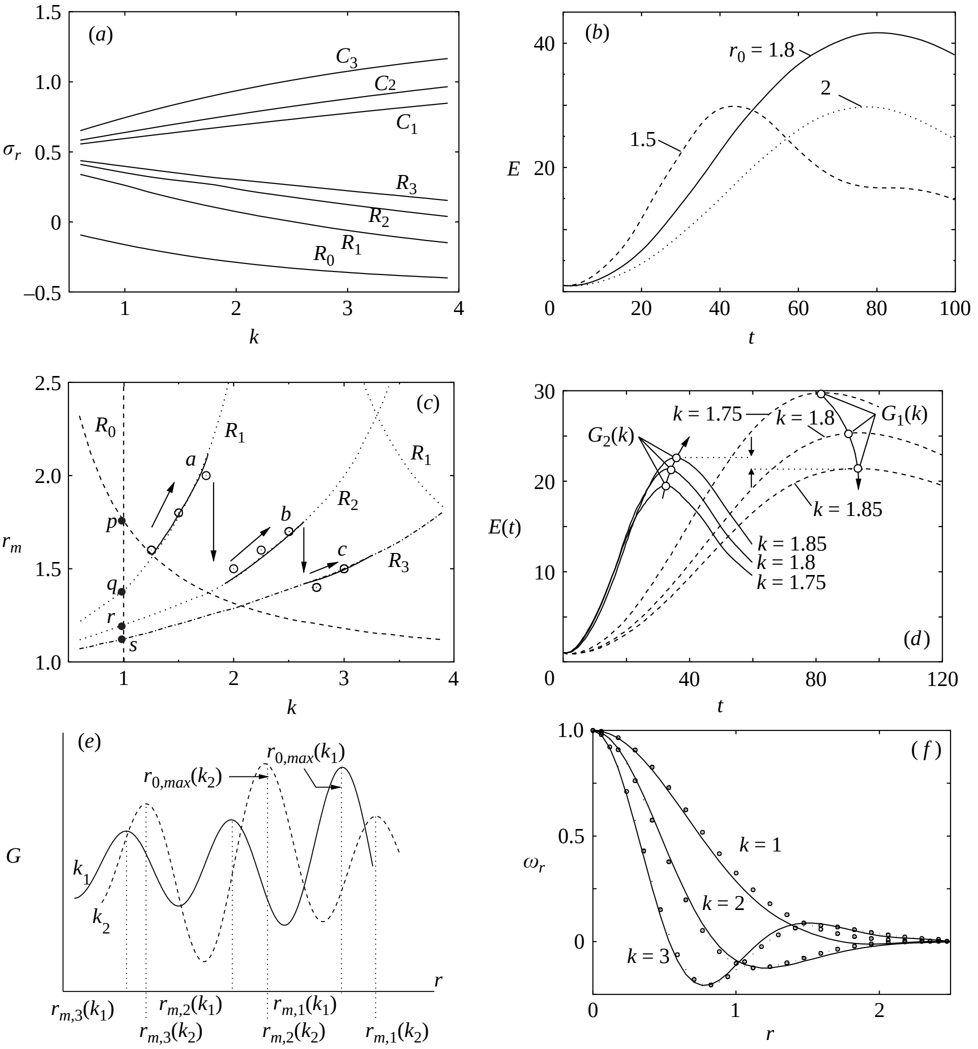

FIGURE 21. Top-hat vortex behaviour (a–e). (a) Dispersion curves. (b) $E(t)$ evolution as function of ribbon radius r_0, for $k = 1.5$ and $Re = 10^4$. (c) The resonant radii r_m, where the mean-flow angular velocity V/r matches eigenmode frequency σ_r, for various eigenmode branches (broken lines R_0–R_3); circles show the computed ribbon radial locations $r_{0,max}$. Arrows show discrete $r_{0,max}$ jumps across different R_i branches, with solid lines showing the trends of $r_{0,max}$. Core ω_z distributions at modes labelled i, ii, iii are plotted in figure 22. Once again, in this (r, k)-plane, broken lines show $r_m(k)$ and symbols and solid lines denote $r_{0,max}(k)$. (d) $E(t)$ evolution when ribbon radius r_0 equals r_m on R_1 (dashed lines) and on R_2 (solid) branches, for various k. The maximum values of $E(t)$, i.e. G, on R_1 and R_2 branches are indicated by curves with open circles $G_1(k)$ and $G_2(k)$, respectively. (e) Sketch of the variations of G with ribbon radius r_0 at two k values k_1 and k_2. At any k, local maxima of G occur at resonant radii r_m, and the global maximum of G corresponds to $r_{0,max}$. (f) Oseen-vortex optimal mode ω_r profiles at time of peak amplification (lines), and Oseen-vortex eigenmode ω_r (symbols), at three k values.

in the core and decreases to zero as $r \to \infty$. Thus, retro-grade eigenmodes with $\sigma_r > 0$ (hence, rotating in the same direction as the mean flow) have oscillation frequencies in the range of fluid angular velocities outside the core.

Perturbation vorticity evolution. To study transient growth in the top-hat vortex, we construct a perturbation vorticity field of the form

$$\left.\begin{aligned}\omega_r &= k\exp\left(-\frac{(r-r_0)^2}{\delta_r^2}\right)\sin(\theta+kz),\\ \omega_\theta &= 0,\\ \omega_z &= \frac{1}{r}\left(1-2r\frac{r-r_0}{\delta_r^2}\right)\exp\left(-\frac{(r-r_0)^2}{\delta_r^2}\right)\cos(\theta+kz).\end{aligned}\right\} \tag{4.9}$$

This field, shown in figure 20(*b*), is in the form of helical, annular 'ribbons' of vorticity centred at $r=r_0$. The vortex lines form closed loops that lie in θ-planes, since ω_θ is identically zero. The perturbation vorticity field after some evolution is shown in figure 20(*c*). The tilting of ω_r into ω_θ and the rapid growth of the azimuthal component is evidenced by the geometry of the computed vortex lines, which are now predominantly azimuthal. The presence of ω_θ implies $uv>0$ Reynolds stress, which causes energy growth.

Recall from figure 18 that core vorticity dynamics comprise (*a*) the growth of *externally induced* $\boldsymbol{\omega}_\perp$ $(=\omega_r\hat{r}+\omega_\theta\hat{\theta})$ induced by azimuthal vortex ribbons outside the core, containing ω_θ; and (*b*) *self-tilting* rotation of $\boldsymbol{\omega}_\perp$ through the combined effects of its azimuthal advection by the mean flow and tilting of mean axial vorticity $\boldsymbol{\Omega}$ into the (r,θ)-plane by perturbation velocity gradients. Now, if the core vorticity perturbation was dominated by a single eigenmode of the vortex, the rate of self-tilting of $\boldsymbol{\omega}_\perp$ would be close to the eigenmode's oscillation frequency σ_r. Further, if this rate of self-tilting matches the mean-flow fluid angular velocity V/r at the ribbon radius r_0, the externally induced $\boldsymbol{\omega}_\perp$ will also advect azimuthally with the same rotational frequency. This is the *resonance mechanism*, causing $\boldsymbol{\omega}_\perp$ to grow.

Resonant radius. To confirm the above scenario, we study the variation in transient growth of the initial perturbation field (4.9) as the radial location of the external ribbon r_0 is varied, for a few equally spaced k values. Flow evolution is obtained through DNS of the linearized Navier–Stokes equation. Figure 21(*b*) plots the energy evolutions for three different values of ribbon location $r=r_0$, all at $k=1.5$, showing that there exists a ribbon location $r_{0,max}$ when energy amplification is maximum; $r_{0,max}=1.8$ here. Corresponding to each eigenmode oscillation frequency σ_r, there exists a radius r_m (call it 'resonant radius') where the fluid angular velocity V/r equals σ_r. At each k, since there is a set of discrete eigenfrequencies, there is also a set of discrete resonant radii. For example, at $k=1$, points p, q, r, s (figure 21*c*) denote the resonant radii $r_{m,0}$, $r_{m,1}$, $r_{m,2}$, $r_{m,3}$, respectively. The variations $r_{m,0}(k)$, $r_{m,1}(k)$, $r_{m,2}(k)$, and $r_{m,3}(k)$ are shown as broken lines R_0–R_3. The figure also plots the calculated $r_{0,max}$ (circles), with solid lines indicating the trends on the different R_i branches. Clearly, there is good agreement between the two radii, r_m and $r_{0,max}$. That is, when the ribbon is located at the resonant radius, the energy growth is the largest, because the externally induced tilting of $\boldsymbol{\omega}_\perp$ and its self-tilting mutually reinforce each other (i.e. resonance) as they are identically aligned. If they were not aligned, there could still be growth (e.g. see $r_0=1.5$ and $r_0=2$ curves in figure 21*b*), but not resonance.

The phenomenon of a vortex wave resonating with external perturbations localized at the resonant radius r_m has been encountered in the context of the axisymmetrization of a perturbed two-dimensional vortex (e.g. Schecter *et al.* 2000) and the three-dimensional interaction between buoyancy waves and vortex Rossby waves in geophysical vortices (Schecter & Montgomery 2004). (These studies refer to the r_m location as the 'critical radius'.) The relevance of the physics of radially localized perturbations discussed here to these studies deserves further analysis.

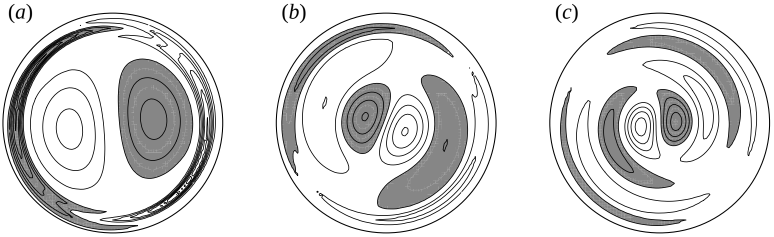

FIGURE 22. ω_z contours at time of peak energy amplification in the top-hat vortex: (*a*) $k = 1.5$, (*b*) $k = 2.5$, and (*c*) $k = 3$, corresponding to the symbols i, ii, iii, respectively, in figure 21(*c*). In each case, r_0 in the initial perturbation field (4.9) equals the corresponding $r_{0,max}$.

Wavenumber dependence of resonant radius. The arrows in figure 21(*c*) show how $r_{0,max}$ increases as k is increased, until a k value is reached where $r_{0,max}$ drops down to the next, higher-order R_i branch. To understand this behaviour, we compare the energy evolutions of two perturbations: the first with ribbon radius $r_0 = r_{m,1}$, the resonant radius on the R_1 branch; and the second with $r_0 = r_{m,2}$, the resonant radius on the R_2 branch. The respective gains (i.e. maxima of the energy curves) are denoted G_1 and G_2 in figure 21(*d*). For small values of k (say, $k = 1.75$) where $r_{0,max} \approx r_{m,1}$, energy with the ribbon at $r_{m,1}$ becomes larger than that with the ribbon at $r_{m,2}$, i.e. $G_1 > G_2$. This is borne out by the $E(t)$ curves (for $k = 1.75$) in figure 21(*d*). It is seen that energy grows more slowly for the $r_{m,1}$ perturbation and, also, attains its maximum value at a larger time. The slower growth is because of the weaker strain rate at $r_{m,1}$ and the longer period of growth due to the smaller vorticity-to-strain ratio. Now, we increase k (correspondingly, also $r_{m,1}$ and $r_{m,2}$) and consider the variations of G_1 and G_2. Note that both $r_{m,1}$ and $r_{m,2}$ increase with increasing k. Figure 21(*d*) plots the energy evolutions for the perturbation pairs at two higher k values ($k = 1.8$ and 1.85) also. With increasing k, G_2 increases and G_1 decreases. G_2 increases because as k increases, $r_{m,2}$ increases, and hence the effect of mean vorticity is weakened. G_1 decreases due to the combined effects of (*a*) slower growth due to the decreased strain rate, and (*b*) more rapid viscous damping due to increased k. As a result of these trends of G_1 and G_2 variations, there is a k value at which G_1 is no longer larger than G_2 (see $k = 1.85$ curves in figure 21*d*). Hence, the optimal ribbon location $r_{0,max}$ jumps down from $r_{m,1}$ to $r_{m,2}$; similarly from $r_{m,2}$ to $r_{m,3}$ at still higher k, and so on.

In summary, the discrete jumps of $r_{0,max}$ in figure 21(*c*) are the result of gradual variation (with k) of the gains experienced by the imposed external vorticity perturbations (ribbons) placed at different resonant radii.

Optimal ribbon radius $r_{0,max}$. It is useful to re-emphasize that corresponding to each k there is a discrete set of resonant radii r_m. There is large volume-integrated energy growth when the ribbons are placed at these radii r_m. As the ribbon radius is continuously varied, so is the energy gain G. Corresponding to each r_m there is a local maximum of the gain curve $G(r)$ (figure 21*e*). At small k (k_1 in the figure), the global maximum of $G(r)$ occurs at the largest resonant radius $r_{m,1}$. As k is increased, the relative magnitudes of the local maxima of $G(r)$ change, and the global $G(r)$ maximum jumps to the next (smaller) resonant radius $r_{m,2}$ at $k = k_2$.

According to figure 21(*c*), as k increases the R_i branch on which the excited eigenmode lies should vary (from R_1 to R_2 to R_3, etc.). The number of radial oscillations of eigenmodes increases with increasing R_i, and the core perturbation vorticity field should become increasingly oscillatory with increasing k. This is indeed the case, as shown in figure 22, where ω_z contours in the vortex core are plotted for

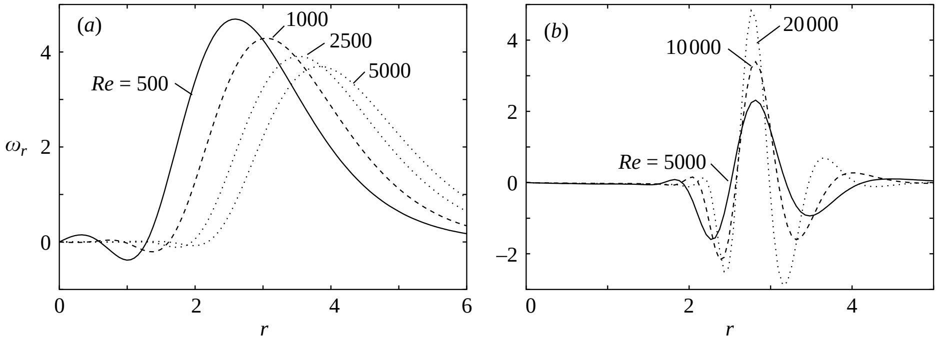

FIGURE 23. Variation of ω_r profiles with Re for (a) $m=0$ and (b) $m=1$ modes. Here $k=1.5$ and the modes are the Oseen-vortex global optimals.

three different values of k, each at the time of peak energy amplification. The vorticity fields are nearly identical to those of the corresponding eigenmodes in figure 21(c).

Such resonant growth of transient perturbations also appears to be qualitatively valid for the Oseen vortex. (Note that the ω evolution here is more complex than that for the top-hat vortex. In the Oseen vortex, $\boldsymbol{\omega}$ evolution outside the core also involves the tilting of mean vorticity Ω into the (r,θ)-plane by the perturbation strain field.) The Oseen vortex optimal modes excite wave-like motions in the core (see e.g. figure 17c–e), with the core vorticity dominated by one particular eigenmode. To illustrate this, figure 21(f) plots ω_r profiles at the time of peak energy, for the global optimal modes at three different k values. It can be seen that these profiles match closely the eigenmode profiles, and that eigenmodes with increasing radial structure are excited as k increases.

Oseen vortex resonance. The preceding results suggest that the bending-wave global optimal modes, which are radially localized outside the vortex core (figure 15), should prefer a radial location where resonant forcing of core waves is possible. Furthermore, since eigenmode σ_r varies very little with Re, so also does the preferred radius. The optimal modes should therefore converge to this preferred radius as Re is increased. Such behaviour contrasts with that of axisymmetric modes, which move to $r \to \infty$ in the limit of infinite Re. This Re-dependence of mode structure is verified by the linear analysis. In figure 23(a), we plot the variation of $m=0$ global optimal mode ω_r-profiles as Re is increased. The axisymmetric modes drift farther from the vortex core, i.e. to regions of weaker vorticity-to-strain ratio, so that the time before growth arrest due to wave generation is increased (as discussed in § 4.2.1). In contrast, the bending wave modes (figure 23b) are increasingly localized about a fixed radial location. With increasing Re, the reduced viscous damping allows even sharply localized modes – with thin regions of opposite-signed ω_r layers – to experience significant growth.

In summary, these results indicate that bending wave optimals are more relevant than axisymmetric modes in high-Re practical flows because they have both large growths and large growth rates (as they are located close to the vortex core). In contrast, axisymmetric optimals feature only large growths and not large growth rates. Therefore, bending waves are likely to be dominant.

Core fluctuation energy. While the growth mechanisms for axisymmetric and bending wave modes are qualitatively similar, there is a sharp contrast in the radial distribution of the perturbation kinetic energy. The axisymmetric modes concentrate energy outside the vortex core, close to the radial location of the initial perturbation (chosen

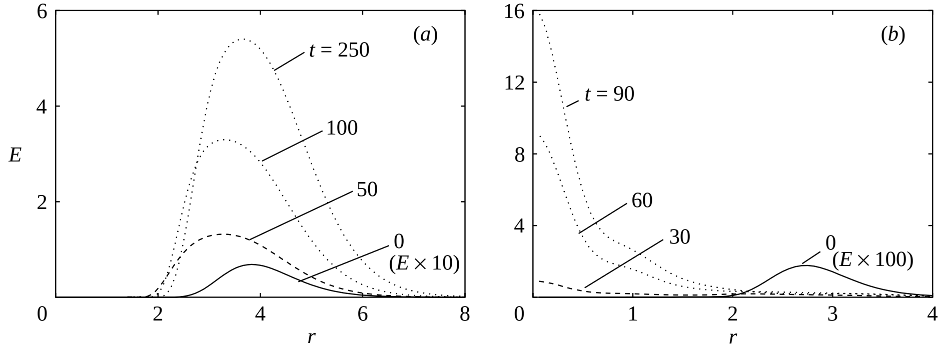

FIGURE 24. Evolution of perturbation energy r-profiles for (a) $m = 0$, $t = 250$ optimal, (b) $m = 1$, $t = 90$ optimal. Both modes are the corresponding Oseen-vortex global optimals. The $t = 0$ profiles have been amplified to reveal the initial distribution. $k = 1.4$ and $Re = 5000$.

to be the location of the global optimal, $r \approx 4$); bending waves generate strong growth of near-axis perturbation. This is illustrated for $m = 0$ and $m = 1$ optimal modes in figure 24. Note that the $E(r)$ profiles are shown only until their maximum growth; subsequently, $E(r)$ profiles decay in both cases. The growth of perturbation energy in the core leads to significant deformation of the vortex column, as seen in figure 17(*p*–*t*).

Similar growth of bending waves has been observed in numerical simulations of a vortex interacting with ambient turbulence (Melander & Hussain 1993). It appears plausible that the strong excitation of bending waves results through transient growth. While the well-organized, spiral patterns of the optimal perturbations (see e.g. figure 17) are uncharacteristic of developed turbulence, it is clear that weak vorticity patches present in a turbulent ambient are wrapped around the vortex column as spiral filaments having vorticity fields similar to that seen in the figure. With the intensification of filament vorticity through stretching by the mean flow, such filaments may dominate the turbulence structure in the vicinity of the large-scale vortex column. The wrapped structure may contribute streamlines of either positive or negative tilt, depending on the direction of the filament's self-induced motion (as illustrated by the simulations of a weak vortex ring in the vicinity of a vortex column, in Marshall & Beninati 2000). The role of transient growth in vortex–turbulence interaction needs further study. The significance of core energy growth lies in possible vortex transition (hence enhanced vortex decay) triggered by weak turbulence surrounding a vortex. The prediction of turbulence-enhanced vortex decay rates remains a challenging problem for turbulence models (see e.g. Wallin & Girimaji 2000), and it appears that the pursuit of optimal perturbations into the nonlinear regime will provide the basis for improved modelling of vortex–turbulence interaction.

5. Concluding discussion

We have shown that the physically relevant Oseen vortex, which is normal-mode stable, allows significant (algebraic) growth of perturbations; such growth will clearly be possible in vortices of other profiles as well. Transient growth in the flow is not restricted to the bending wave, but occurs for waves of arbitrary azimuthal wavenumbers m. The physical mechanisms underlying such growth have been elucidated here. Two distinct mechanisms exist, which – studied here in detail for the limiting cases of two-dimensional (axial wavenumber $k = 0$) and axisymmetric ($m = 0$) perturbations – act in tandem ($m, k \neq 0$). The first, two-dimensional, mechanism involves the growth of perturbations with positive-tilt streamlines (contributing positive uv). Growth is arrested inviscidly when the differential advection of axial vorticity by the mean flow transforms the streamlines to predominantly negative tilt. In the second mechanism, three-dimensional perturbations grow through the tilting of radial vorticity into the azimuthal direction and subsequent stretching of ω_θ. The radial motions induced by azimuthal vortex filaments generate $uv > 0$, hence causing growth. There is some similarity between the growth mechanisms in a vortex and in plane shear flows, where two-dimensional 'shearing' and three-dimensional 'lift-up' mechanisms of growth have been found previously (see e.g. Farrell & Ioannou 1993). However, rotating flows differ from plane shear flows in one important respect. Rotating flows feature spatial separation between regions of large vorticity and large strain. The perturbation vorticity dynamics in these two regions are quite different: whereas monotonic growth of perturbation vorticity is possible in regions of pure strain, rotation-dominated regions limit transient growth by coupling all three vorticity components and generating wave motion, such as core dynamics. Such wave motion, inviscidly, limits transient growth.

We have investigated the parametric dependence of transient growth on m, k and Re. As expected, the damping effects of viscosity cause energy amplification to decrease with increasing k or m and also with decreasing Re. At given k and Re, axisymmetric modes ($m = 0$) exhibit the largest growth. For $m = 0$ modes, numerical results, supported by physical arguments, indicate that there is no upper bound for transient growth in the inviscid limit. However, the largest growing modes are also the slowest growing, since such modes are localized at increasingly large distances from the vortex core and hence in regions of very weak strain rate. This is expected to limit the extent of transient growth in practical flows for two reasons. First, faster growing modes can attain amplitudes where nonlinear effects become significant and, possibly, limit the linear-regime growth of the slower growing modes. Second, vortices in practical flows are never truly isolated, but are either in the vicinity of walls or of other vortices. Thus, a perturbation located far away from a vortex is of limited physical significance.

In contrast to $m = 0$ modes, bending wave ($|m| = 1$) optimal modes do not shift to $r \to \infty$ with increasing growth. These are localized at a preferred radius, close to the vortex column core, where resonant excitation of core waves occurs. Resonance-driven transient growth, demonstrated herein via a simplified Rankine-like (top-hat) vortex model, leads to strong growth of *core* fluctuation energy. This mechanism explains why strong bending waves are excited on a vortex interacting with ambient turbulence. Growth of core waves is potentially significant in turbulent flows, since it will probably result in vortex core transition. Excitation of such waves may prove useful in ameliorating the aircraft wake hazard problem.

The present results lead obviously to the question of how nonlinear effects alter the growth of optimal perturbations, and whether transient growth leads to fully developed and self-sustaining turbulence, as in the case of plane shear flows. These questions are currently being investigated via direct numerical simulation. While experiments (Phillips & Graham 1984) and numerical simulations (Risso & Corjon 1997) suggest that turbulence, when present, has a significant effect on vortex decay, it remains unclear whether an isolated vortex can sustain turbulence. Spalart (1998) notes that the failure of numerical simulations (such as Sreedhar & Ragab 1994) to find sustained turbulence could be due to the inappropriate initial conditions chosen. The framework of optimal perturbations addressed here should provide the appropriate physical understanding and computational initial conditions to address the modelling of a turbulent vortex.

REFERENCES

Antkowiak, A. & Brancher, P. 2004 Transient growth for the Lamb-Oseen vortex. *Phys. Fluids* **16**, L1.

Arendt, S., Fritts, D. & Andreassen, O. 1997 The initial value problem for Kelvin vortex waves. *J. Fluid Mech.* **344**, 181.

Ash, R. L. & Khorrami, M. R. 1995 Vortex stability. In *Fluid Vortices* (ed. S. I. Green), p. 317. Kluwer.

Butler, K. M. & Farrell, B. F. 1992 Three-dimensional optimal perturbations in viscous shear flow. *Phys. Fluids* A **4**, 1637.

Canuto, C., Hussaini, M. Y., Quarteroni, A. & Zang, T. A. 1988 *Spectral Methods in Fluid Dynamics*. Springer.

Corbett, P. & Bottaro, A. 2000 Optimal perturbations for boundary layers subject to stream-wise pressure gradient. *Phys. Fluids* **12**, 120.

Crouch, J. D. 1997 Instability and transient growth for two trailing vortex-pairs. *J. Fluid Mech.* **350**, 311.

Fabre, D., Jacquin, L. & Loof, A. 2002 Optimal perturbations in a four-vortex aircraft wake in counter-rotating configuration. *J. Fluid Mech.* **451**, 319.

Farrell, B. F. 1988 Optimal excitation of perturbations in viscous flow. *Phys. Fluids* **31**, 2093.

Farrell, B. F. & Ioannou, P. J. 1993 Optimal excitation of three-dimensional perturbations in viscous constant shear flow. *Phys. Fluids* A **5**, 1390.

Gustavsson, L. H. & Hultgren, L. S. 1980 A resonance mechanism in plane Couette flow. *J. Fluid Mech.* **98**, 149.

Kerswell, R. R. 2002 Elliptical instability. *Annu. Rev. Fluid Mech.* **34**, 83.

Lessen, M. R., Singh, P. J. & Paillet, F. 1974 The stability of a trailing line vortex. Inviscid theory. *J. Fluid Mech.* **63**, 753.

Marshall, J. S. & Beninati, M. L. 2000 Turbulence evolution in vortex dominated flows. In *Nonlinear Instability, Chaos and Turbulence II*. Advances in Fluid Mechanics, vol. 25 (ed. L. Debnath & D. N. Riahi), p. 1. WIT Press.

Mayer, E. W. & Powell, K. G. 1992 Viscous and inviscid instabilities of a trailing vortex. *J. Fluid Mech.* **245**.

Melander, M. V. & Hussain, F. 1993 Coupling between a coherent structure and fine-scale turbulence. *Phys. Rev.* E **48** (4), 48.

Melander, M. V. & Hussain, F. 1994 Core dynamics on a vortex column. *Fluid Dyn. Res.* **13**, 1.

Michalke, A. & Timme, A. 1967 On the inviscid instability of certain two-dimensional vortex-type flows. *J. Fluid Mech.* **29**, 647.

Miyazaki, T. & Hunt, J. C. R. 2000 Linear and nonlinear interactions between a columnar vortex and external turbulence. *J. Fluid Mech.* **402**, 349.

Montgomery, M. T. & Kallenbach, R. J. 1997 A theory for vortex rossby-waves and its application to spiral bands and intensity changes in hurricanes. *Q. J. R. Met. Soc.* **123**, 435.

Nolan, D. S. & Farrell, B. F. 1999 The intensification of two-dimensional swirling flows by stochastic axisymmetric forcing. *J. Atmos. Sci.* **56**, 3937.

Phillips, W. R. C. & Graham, J. A. H. 1984 Reynolds-stress measurements in a turbulent trailing vortex. *J. Fluid Mech.* **147**, 353.

Pradeep, D. S. & Hussain, F. 2004 Effects of boundary condition in numerical simulations of vortex dynamics. *J. Fluid Mech.* **516**, 115.

Reddy, S. C. & Henningson, D. S. 1993 Energy growth in viscous channel flow. *J. Fluid Mech.* **252**, 209.

Rennich, S. C. & Lele, S. K. 1997 Numerical method for incompressible vortical flows with two unbounded directions. *J. Comput. Phys.* **137**, 101.

Risso, F. & Corjon, A. 1997 Direct numerical simulations of wake vortices in intense homogeneous turbulence. *AIAA J.* **35**, 1030.

Saffman, P. G. 1992 *Vortex Dynamics*. Cambridge University Press.

Schecter, D. A., Dubin, D. H. E., Cass, A. C., Driscoll, C. F., Lansky, I. M. & O'Neil, T. M. 2000 Inviscid damping of asymmetries on a two-dimensional vortex. *Phys. Fluids* **12**, 2397.

Schecter, D. A. & Montgomery, M. T. 2004 Damping and pumping of a vortex rossby wave in a monotonic cyclone: critical layer stirring versus inertia-buoyancy wave emission. *Phys. Fluids* **16**, 1334.

Schmid, P. J. & Henningson, D. S. 2001 *Stability and Transition in Shear Flows*. Springer.

Schmid, P. J., Henningson, D. S., Khorrami, M. R. & Malik, M. R. 1993 A study of eigenvalue sensitivity for hydrodynamic stability operators. *Theoret. Comput. Fluid Dyn.* **4**, 227.

Schoppa, W. & Hussain, F. 2002 Coherent structure generation in near-wall turbulence. *J. Fluid Mech.* **453**, 57.

Smith, R. A. & Rosenbluth, M. N. 1990 Algebraic instability of hollow electron columns and cylindrical vortices. *Phys. Rev. Lett.* **64**, 649.

Spalart, P. 1998 Aircraft trailing vortices. *Ann. Rev. Fluid. Mech.* **30**, 107.

Sreedhar, M. & Ragab, S. 1994 Large eddy simulation of longitudinal stationary vortices. *Phys. Fluids* **6**, 2501.

Trefethen, L. N. 1992 Pseudospectra of matrices. In *Numerical Analysis 1991*, p. 234. Longman.

Trefethen, L. N., Trefethen, A. E., Reddy, S. C. & Driscoll, T. A. 1993 Hydrodynamic stability without eigenvalues. *Science* **261**, 578.

Wallin, S. & Girimaji, S. S. 2000 Evolution of an isolated turbulent trailing vortex. *AIAA J.* **38**, 657.